ISSN 0030-400X, Optics and Spectroscopy, 2021, Vol. 129, No. 7, pp. 707–736. © Pleiades Publishing, Ltd., 2021.
ISSN 0030-400X, Optics and Spectroscopy, 2021. © Pleiades Publishing, Ltd., 2021.
Russian Text © The Author(s), 2021, published in Optika i Spektroskopiya, 2021, Vol. 129, No. 5, pp. 569–598.

Spectral and Amplitude–Time Characteristics of the Cherenkov Radiation upon Excitation of Transparent Materials by an Electron Beam

V. F. Tarasenko[a], *, E. Kh. Baksht[a], **, M. V. Erofeev[a], *, and A. G. Burachenko[a], ******

[a] *Institute of High Current Electronics, Siberian Branch, Russian Academy of Sciences, Tomsk, 634055 Russia*

**e-mail: VFT@loi.hcei.tsc.ru*

***e-mail: BEH@loi.hcei.tsc.ru*

****e-mail: MVE@loi.hcei.tsc.ru*

*****e-mail: BAG@loi.hcei.tsc.ru*

Received December 21, 2020; revised January 22, 2021; accepted February 1, 2021

Abstract—The interest in studying characteristics of the Vavilov–Cherenkov radiation (VCR) increased in connection with works on creation of runaway electron (RE) detectors for tokamak type facilities. The survey presents results of investigations of spectral, amplitude–time, and spatial VCR characteristics obtained mainly in recent years upon excitation of transparent substances by a flux of electrons with energies of tens or hundreds of kiloelectronvolts. The VCR spectra in diamond (natural and synthetic), quartz glass, sapphire, and leucosapphire are presented. It is reported about VCR detection in MgF_2, Ga_2O_3, and other transparent samples. The spectra and amplitude–time characteristics of VCR and pulsed cathodoluminescence (PCL) are compared at different electron energies. For some samples, VCR spectra are calculated with allowance for dispersion of the refractive index, as well as energy distributions of beam electrons and decreases in energy of electrons in the process of their deceleration in the substance of the samples. The emission spectrum of polymethylmethacrylate (PMMA) which is used as a material for radiators in Cherenkov detectors and lightguides transmitting the radiation in scintillation dosimeters and as a plastic base in organic scintillators is studied.

Keywords: Vavilov–Cherenkov radiation, pulsed cathodoluminescence, electron beam, photoexcitation

DOI: 10.1134/S0030400X21050167

1. INTRODUCTION

In recent years, there increased the number of works devoted to investigations of luminescence of different substances under the action of electron beams. In particular, great attention is paid to studying and analyzing characteristics of Cherenkov radiation [1] upon excitation of samples of different materials by electron beams with energies of tens or hundreds of kiloelectronvolts, as well as to comparing Cherenkov radiation with characteristics of pulse cathodoluminescence (PCL) under similar conditions. Note that the term "Cherenkov radiation" at present is usually used in foreign literature while Russian-language publications use the term "Vavilov–Cherenkov radiation" (VCR). For this reason, in the Russian-language survey, we use the term VCR.

It is well known that VCR appears when charged particles move in the substance with a speed exceeding the phase speed of light. Vavilov–Cherenkov radiation is universal in the sense that all transparent bodies in the liquid, gaseous, and solid states glow under the action of charged particles with a sufficient energy. This makes it possible to use VCR for detection of different particles. For the VCR appearance, the energy of the particle with a negative or positive charge must exceed the threshold energy which depends on the refractive index of the substance. The VCR intensity increases with an increase in energy of the charged particle; for this reason, VCR is widely used for detecting high-energy particles [2–8], in particular, in investigations of particles permanently bombarding the atmosphere with energies from hundreds of megaelectronvolts to several or tens of gigoelectronvolts [9–12]. VCR detectors for high-energy particles are usually designed using the dependence of angular VCR characteristics in the visible and ultraviolet (UV) spectrum ranges on particle energy. According to the theory [3, 13] which is verified by experimental measurements, VCR propagates at an angle to the direction of the particle motion and this angle depends on the energy and kind of the particle, as well as on the refractive index of the substance. This allows one to diagnose parameters of high-energy electron beams. As an example, experiments [14] demonstrate (by detection of VCR generated in optical fibers) the possibility of measuring the

transverse profile of low-intensity electron beam with energy of several megaelectronvolts. The main advantage of the method described in [14] is the perpendicular orientation of the fiber relative to the axis of the electron beam. This decreases errors in experimental measurements as compared to the case where the optical fiber is inclined at an angle corresponding to the VCR direction. In [15], by means of VCR, the duration of a beam current pulse was measured with a high time resolution using a streak camera; it was equal to ~250 fs.

In the recent decade, great attention is paid to creation of Cherenkov detectors for the detection of runaway electrons (REs) in tokamak type facilities and to investigations of conditions for RE generation in such facilities [16–27]. It was supposed that using VCR for diagnostic purposes would help to determine reasons behind the destruction of walls of the RE vacuum chamber and to understand optimum conditions for obtaining high-temperature plasma. In [28, 29], it was established that the RE energy in tokamak facilities amounted from tens of kiloelectronvolts to tens of megaelectronvolts. At the same time, REs can damage walls of the working chamber [29, 30]. Correspondingly, the created detectors must detect electrons with different energies and preserve their properties at high irradiation doses. For this reason, in [16–19], diamond was used as a radiator in designing VCR detectors. Diamonds have a high refractive index, as well as high thermal conductivity and damage threshold [31]. However, emission spectra of diamond radiators were not recorded in [16–18]. Only in [19] the Cherenkov detector was calibrated at electron energy of 2.3 MeV and the emission spectrum was presented; however, it did not correspond to the VCR spectrum. In the range of 500–700 nm, an intense band with a maximum at a wavelength of 637 nm was observed.

In [32], on irradiation of mica, quartz and $BaTiO_3$, VCR was detected on a facility with an accelerating voltage up to 200 kV. The radiation in mica had an intensity maximum at an electron energy of 200 keV at a wavelength of 400 nm, which corresponds to the VCR spectrum attenuated in the UV range by absorption of the sample. In a later work of the authors [33], it was reported about radiation of thin films of different materials (mica, silicon, and silver). The radiation parameters were determined taking into account the dependence of the radiation intensity on the film thickness and accelerating voltage. Radiation emanating from mica in the direction of the electron beam propagation contained VCR which had an intensity maximum at an electron energy of 200 keV at a wavelength of 300 nm. However, the cause of the decrease in the radiation intensity in the shortwave range was not discussed and the transmission spectrum of mica was not presented. In [34–36], it was shown that the VCR intensity in diamond at electron energies of up to 200 keV was considerably lower than the PCL intensity in the UV and visible spectral ranges and its detection is impeded.

The investigation of PCL without VCR detection was described in many works (e.g., monograph [37] and collected papers [38, 39]). In recent works [34, 35], VCR was detected in synthetic and natural diamonds at electron energies of up to 200 keV, but only with the use of a monochromator and a photomultiplier. The VCR intensity, as it just follows from the theory [3, 13], increased with a decrease in the wavelength in the range of 240–360 nm. However, at electron energy of up to 200 keV, it was difficult to distinguish VCR on the background of cathodoluminescence band emission. The best way for VCR detection at comparatively low electron energies is using samples that are transparent in the UV range and characterized by low intensity or PCL absence in this range.

As should be expected, the VCR intensity increased with an increase in the electron energy. For example, in [40–42], conditions were determined under which VCR was detected at electron energies of up to 200–400 keV using standard spectrometers with CCD line sensor.

It is also interesting to study luminescence of polymethylmethacrylate (PMMA, plexiglas) under the action of an electron beam. This material is widely used in medical dosimetry when determining doses of irradiation by different kinds of ionizing radiation [43–46]. Emission spectra of PMMA were detected in several works devoted to this subject [44, 45, 47]. However, there were no data about emission spectra of PMMA under the direct action of electrons with energy of tens or hundreds of kiloelectronvolts on this material.

Using the PMMA luminescence for estimating the energy in a RE beam was proposed in [48, 49]. Radiation pulses were detected at voltages of not more than 300 kV at a diode filled with atmospheric pressure air; according to authors of [48, 49], they belong to VCR. In addition, the duration of radiation pulses significantly the duration of beam current pulses and PMMA emission spectra were not detected. At the same time, as shown in [50–52], VCR detection at beam electron energies of up to 400 keV in PMMA is impeded even with the use of a monochromator and a photomultiplier due to strong radiation absorption in the range shorter than 300–350 nm, as well as due to the internal breakdown of samples as a result of electron accumulation in them at high beam current densities and/or long pulse durations.

Therefore, results obtained in different research teams on spectral investigations of VCR in diamond, as well as in other substances, were incomplete and required additional investigations, as well as a thorough analysis and comparison with PCL characteristics.

This survey presents results of investigations of spectral, amplitude–time, and spatial emission char-

acteristics of materials transparent in the visible and UV spectral ranges when exciting by a beam of electrons with energies of tens or hundreds of kiloelectronvolts. It also shows conditions under which the VCR intensity exceeds the PCL intensity.

The survey consists of six sections including Introduction and Conclusions. In Section 2, the cause of the VCR appearance is explained at the qualitative level, and main relationships for VCR and properties of this radiation are presented. In Section 3, the experimental equipment used in the investigations is described, parameters of electron accelerators, schemes of experimental setups, and measurement techniques are presented. Section 4 is devoted to the description of investigation results on spectral and amplitude–time characteristics of luminescence excited in samples of different (mainly, crystalline) materials by electron beams with different parameters. In Section 5, investigation results on the interaction between PMMA samples and electron beams are described: amplitude–time and spectral characteristics of luminescence, as well as destruction thresholds. The final section presents summaries of investigation considered in the survey.

2. PROPERTIES OF THE VAVILOV–CHERENKOV RADIATION

2.1. History of the Discovery

In 1934, P.A. Cherenkov, an experimental physicist (at that time, a postgraduate under supervision of Academician S.I. Vavilov), investigated luminescence of liquids under the action of radium gamma radiation and discovered a new kind of luminescence. The report about this discovery was published by Cherenkov and Vavilov in [53, 54]. In experimental investigations of the new kind of luminescence, Cherenkov could establish that the luminescence appeared owing to electrons forming as a result of the Compton effect of radium gamma radiation on atomic electrons of the substance. The glow in different liquids appeared only on irradiation by hard gamma radiation and was absent on irradiation by a softer X-ray radiation (i.e., the luminescence was of threshold character). In contrast to luminescence, neither temperature quenching nor impurity quenching was observed. In addition, the observed glow was blue (the highest radiation intensity was concentrated in the blue-violet spectral range), strongly pronounced directionality (along the direction of motion of Compton electrons), and strongly polarized (differed from the luminescence polarization). In 1937, three years after the discovery of this glow, Soviet theoretical physicists I.E. Tamm and I.M. Frank created a theory which completely explains the VCR physical mechanism [55].

2.2. Main VCR Properties

The VCR appearance and its directionality can be explained at the qualitative level by the Huygens–Fresnel principle. Let us consider the electron motion in a transparent medium under the assumption that all reasonings presented below are related to any charged particle. When an electron moves with a velocity v in a transparent medium with a refractive index $n > 1$, there appears a short-time polarization of the substance near the trajectory of the moving electron. After the electron moves away from the considered region, polarized molecules or atoms return to their initial unperturbed state. This process is accompanied by electromagnetic radiation in the medium. If the electron moves in an optically isotropic medium, spherical electromagnetic waves will radiate along its trajectory. The phase propagation speed of such electromagnetic waves in a medium with a refractive index n is determined as

$$u = \frac{c}{n}, \tag{1}$$

where c is the speed of light in vacuum.

In the case where $v < u$, waves emitted along the whole trajectory at any point at a distance from the trajectory will interfere and yield the zero amplitude of the electromagnetic field. If the electron velocity v is higher than the propagation speed of electromagnetic waves u in this medium (Fig. 1a), then the envelope of the appearing spherical waves forms a wavefront with a nonzero amplitude of the electromagnetic field.

The wavefront is a conical surface with a vertex at a point coinciding with the instantaneous position of the electron. On this conical surface, the condition of coherence for elementary spherical waves is satisfied. Normals to the wavefront (wave vectors **k** depicted in Fig. 1a) show the direction of VCR propagation. The angle θ constituted by the direction of the electron motion and the wave vector can be calculated proceeding from the following considerations. The electron passing the point A (Fig. 1a) generates a spherical electromagnetic wave which propagates to the distance $R = AC = ut$ during time t. During the same time, the electron moving with the velocity $v > u$ passes the distance $AB = vt$.

Therefore, the VCR propagation angle θ is determined from the expression

$$\cos\theta = \frac{AC}{AB} = \frac{u}{v} = \frac{c}{nv} = \frac{1}{\beta n}, \tag{2}$$

where $\beta = v/c$.

Radiation appearing at each point of the trajectory propagates along the surface of a cone (Fig. 1b) the vertex of which is positioned at this point, the axis coincides with the electron trajectory, and the plane angle at the vertex is equal to 2θ. This cone is often called the Cherenkov cone or the VCR cone.

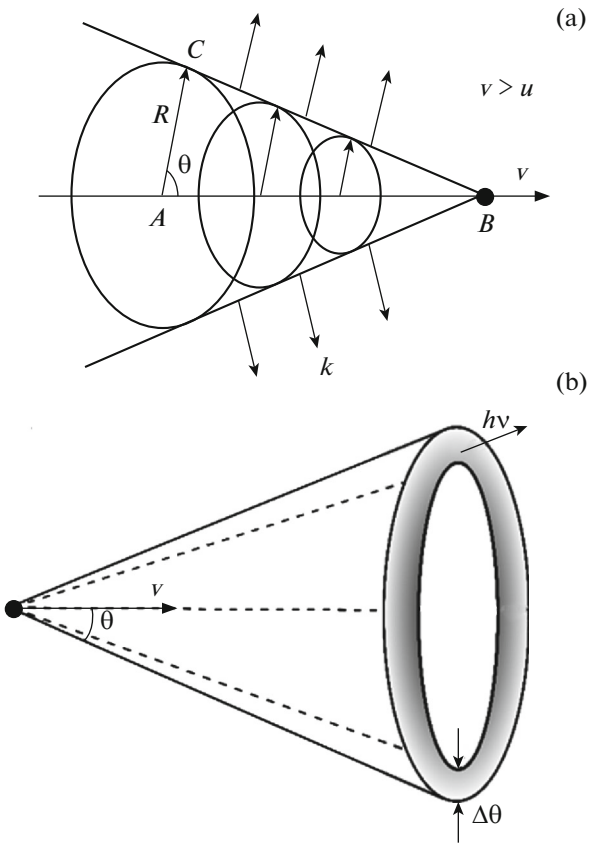

Fig. 1. (a) Formation of the wavefront of the Vavilov–Cherenkov radiation and (b) the Cherenkov cone.

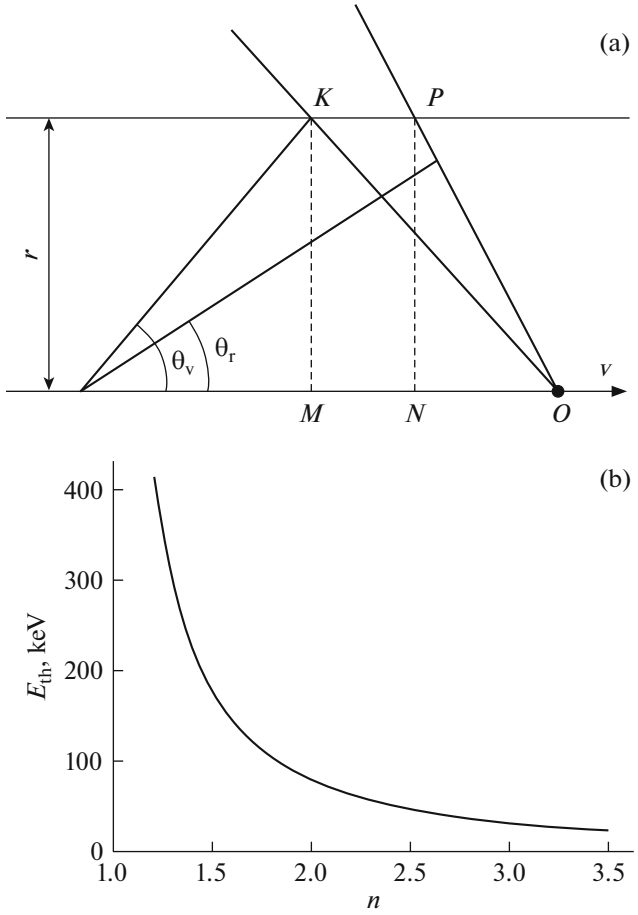

Fig. 2. (a) Formation of the finite VCR duration. (b) Threshold electron energy for the appearance of VCR as a function of the refractive index of the medium.

Measuring the angle θ and knowing the refractive index of the medium, one can calculate the velocity and, therefore, the energy of the electron. The higher the electron velocity and/or the refractive index n of the medium, the larger the VCR propagation angle θ. The maximum possible angle at which VCR can propagate in a medium with a refractive index n can be determined from formula (2) at $\beta = 1$. For example, for water ($n = 1.33$) this angle is $\theta_{max} \approx 41°$; for diamond ($n = 2.42$), $\theta_{max} \approx 66°$. If the particle trajectory length l in the medium is comparable with the VCR wavelength λ, diffraction effects become significant and VCR propagates within the range of angles θ and $\theta + d\theta$, where $d\theta \approx \frac{\lambda}{l}\sin\theta$ [56].

The refractive index of a real medium n depends on the radiation wavelength λ; therefore, angle θ in expression (2) varies depending on λ. In the case of normal dispersion, the refractive index of light in the violet spectral range n_v is larger than in the red range n_r; therefore, angles θ for the red and violet light are different. The angle at which VCR propagates will be blurred by the quantity $\Delta\theta = \theta_v - \theta_r$ (Fig. 1b). Therefore, VCR appearing at each small fragment of the electron trajectory will propagate between two conical surfaces (the region highlighted in gray in Fig. 1b), where the outer cone corresponds to the VCR propagation in the violet range of the spectrum and the inner cone corresponds to the propagation in the red range.

The angular width of the Cherenkov cone can be also affected by multiple electron scattering in the medium. When an electron beam passes through a medium with a thickness T, this influence can be estimated as [41, 56] $\Delta\theta_a \approx \sqrt{\theta_{ms}^2 + \theta_e^2}$, where θ_{ms} is the root-mean-square angle of multiple scattering at the length $T/2$ and θ_e is the initial divergence of the electron beam. At high electron energies, as well as at small values of T and divergence of the electron beam, $\Delta\theta_l \to 0$.

Due to dispersion of the refractive index, radiation at different wavelengths will arrive at the observation point P at different times (Fig. 2a): if the electron located at a point O moves along the trajectory MO, the front corresponding to the violet spectral range (OK) will arrive later than the front corresponding to the red spectral range (OP)). The delay is determined

by the time during which the violet front is displaced along the direction *KP* by a distance equal to the length of the segment *KP*. Since the displacement speed of the violet (and red) front along the direction *KP* is equal to the motion velocity of the electron ($KP \parallel MO$), the delay time is determined as

$$\Delta t = \frac{KP}{v} = \frac{MO - NO}{v} = \frac{r}{v}(\tan\theta_v - \tan\theta_r),$$

provided that $KM \perp MO$, $PN \perp MO$.

In the general case,

$$\Delta t = \frac{r}{v}(\tan\theta_2 - \tan\theta_1),$$

where θ_1 and θ_2 are angles corresponding to boundary lengths of VCR waves (determined by the transparent region of the medium). The quantity Δt is estimated [57] as ~10^{-12}–10^{-11} s. Therefore, the Vavilov–Cherenkov effect can provide a very high time resolution. This distinguishes VCR from luminescence which as a rule has an incomparably longer decay time.

When moving in a substance, the electron spends a part of its energy for VCR, although this part is small (~0.1%) [58] as compared to losses for ionization of substance atoms. The electron energy losses for VCR in the frequency interval $d\omega$ can be determined in terms of the effective force of radiation deceleration dF [57] (the Tamm–Frank formula):

$$dF = \frac{dW}{dt} = \frac{e^2}{c^2}\left(1 - \frac{1}{\beta^2 n(\omega)^2}\right)\omega d\omega, \qquad (3)$$

where $\frac{dW}{dt}$ are electron energy losses for VCR per unit path length, e is the electron charge, and ω is the cyclic frequency.

For a multicharged particle, a multiplier Z^2 is added. It determines the particle charge:

$$dF = \frac{(Ze)^2}{c^2}\left(1 - \frac{1}{\beta^2 n(\omega)^2}\right)\omega d\omega. \qquad (4)$$

One can pass in Eq. (3) from the cyclic frequency ω to the wavelength λ using the formula $\omega = 2\pi c/\lambda$. Then, the spectral density of the VCR power $dP(\lambda)/d\lambda$ for a single electron can be determined from the expression

$$dP(\lambda) = v dF = 4\pi^2 e^2 v\left(1 - \frac{1}{\beta^2 n^2(\lambda)}\right)\frac{d\lambda}{\lambda^3}. \qquad (5)$$

Dividing the right-hand and left-hand sides of Eq. (5) by $d\lambda$ and multiplying them by the corresponding time interval dt, we obtain an expression for the spectral density of the radiation energy $dE/d\lambda$.

Dividing the right-hand and left-hand sides of the Tamm–Frank formula (4) by the quantum energy $h\nu$ and neglecting the dispersion of the refractive index, it is easy to obtain that the number of VCR quanta emitted by a charged particle in the medium at a path length l in a spectral range defined by wavelengths λ_1 and λ_2 (provided that β only slightly varies at the length l) is equal to

$$N_{h\nu} = 2\pi\alpha l Z^2\left(\frac{1}{\lambda_1} - \frac{1}{\lambda_2}\right)\left(1 - \frac{1}{\beta^2 n^2}\right) = 2\pi\alpha l Z^2\left(\frac{1}{\lambda_1} - \frac{1}{\lambda_2}\right)\sin^2\theta, \qquad (6)$$

where α is the fine structure constant $\left(\alpha = \frac{e^2}{\hbar c} = \frac{1}{137}\right)$.

In the visible spectral range, the intensity of VCR excited by an electron prevails over the intensity of bremsstrahlung radiation. In [57], based on the analysis of main formulas for VCR and bremsstrahlung radiation, it is concluded that the ratio of VCR and bremsstrahlung radiation intensities in the visible spectral range is ~10^4 for almost all electron energies. As an example, in [57], the number of photons emitted by an electron with an energy of 10 MeV in water due to bremsstrahlung radiation and VCR is compared in the spectral range of 350–700 nm. The number of bremsstrahlung radiation photons emitted at the radiation length (at which the electron energy decreases by a factor of e) in the wavelength range from λ_1 to λ_2 is calculated by the formula [57] $N_{br} = \frac{4}{3}\ln\frac{\lambda_2}{\lambda_1}$. The radiation length in water is ~34 cm; therefore, during the passage of 1 cm of water, the electron emits 3×10^{-2} photons in the spectral range of 350–700 nm due to bremsstrahlung radiation. The number of photons emitted by the electron due to VCR under the same conditions and in the same spectral range according to formula (6) is 263 photons. Thus, the VCR intensity in the visible part of the spectrum exceeds the bremsstrahlung radiation intensity approximately by a factor of 10^4.

The Vavilov–Cherenkov radiation appears beginning from a certain minimal electron energy determined by the refractive index of the substance n. This energy is called the threshold energy. The threshold energy of the VCR appearance at a specific wavelength $E_{th}(\lambda)$ is determined from formula (5) as the multiplier $\left(1 - \frac{1}{\beta^2 n^2(\lambda)}\right)$ is equal to zero and β is expressed in terms of the relativistic kinetic energy of the electron:

$$E_{th}(\lambda) = m_e c^2\left(\frac{n(\lambda)}{\sqrt{n^2(\lambda) - 1}} - 1\right), \qquad (7)$$

where m_e is the mass of the electron at rest.

In practice, when determining E_{th}, dispersion of the refractive index is often neglected: $n(\lambda)$ is replaced by the value of the refractive index for the wavelength of the D-line of the sodium spectrum (589.3 nm) mea-

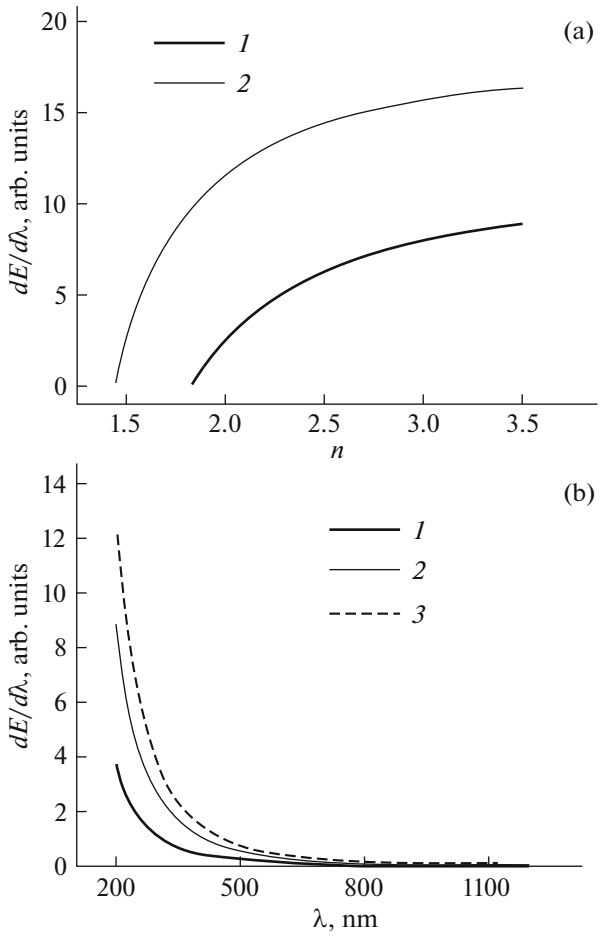

Fig. 3. (a) Spectral power/energy density of VCR as a function of the refractive index for electron energies of (*1*) 100 and (*2*) 200 keV. (b) Spectral power/energy density of VCR in diamond as a function of the wavelength for electron energies of (*1*) 100, (*2*) 200, and (*3*) 300 keV.

sured under atmospheric pressure of air and temperature of 20°C [59]. This refractive index is denoted as n_D or simply n under the assumption that $n = n_D$. The higher the refractive index n, the lower the threshold energy of the VCR appearance E_{th} (Fig. 2b). In particular, for diamond with the refractive index $n = 2.42$, the threshold energy of the VCR appearance $E_{th} =$ 50 keV.

It also follows from Eq. (5) that the VCR intensity increases with a decrease in the wavelength—somewhat faster than $1/\lambda^3$ because the multiplier $\left(1-\frac{1}{\beta^2 n^2(\lambda)}\right)$ also increases with a decrease in λ, although rather slowly. For this reason, the human eye perceives VCR as a blue-violet glow.

The VCR intensity (as well as the spectral energy density) increases also with an increase in the kinetic energy of electrons, as well as with an increase in the refractive index of the medium (Fig. 3). It is seen from Fig. 3b that the largest fraction of the VCR energy is concentrated in the UV spectral range. Therefore, it is easiest to detect VCR in media that are transparent in the UV spectral range and have a comparatively high refractive index.

It is necessary to note that VCR is polarized. The electric field strength vector is directed perpendicularly to the Cherenkov cone surface; the magnetic field strength vector, along the tangent. The radiation polarization was discovered experimentally by Cherenkov [1]; later, it got an explanation in the theory of Tamm and Frank [55]. Analysis of main formulas describing the theory of Vavilov–Cherenkov radiation allows one to formulate its main properties:

- VCR is of threshold (in energy/velocity) character;
- Vavilov–Cherenkov effect, in contrast to luminescence, is almost free from time lag;
- VCR has a pronounced directionality—it propagates at a certain angle to the motion direction of a charged particle;
- there is the maximum angle of VCR propagation for particles with a speed close to the speed of light in the medium;
- VCR is polarized;
- VCR has a continuous spectrum;
- VCR energy is concentrated mainly in the shortwave spectral range;
- VCR, in contrast to luminescence, is susceptible neither to impurity quenching nor to temperature quenching.

3. EXPERIMENTAL EQUIPMENT AND MEASUREMENT TECHNIQUES

3.1. Electron Accelerators Used in Experiments

The spectral, amplitude–time, and spatial characteristics of VCR and PCL excited in transparent dielectrics and semiconductors by an electron beam with an energy of hundreds of kiloelectronvolts were investigated using different accelerators; the operation modes of some accelerators could be changed. This made it possible to vary electron beam parameters in a wide range and to cover the range of electron energies from ~40 to ~400 keV. Parameters of subnanosecond and nanosecond accelerators (we call them according to the name of the used generator) are presented in Table 1 with the indication of the operation modes.

Each accelerator consisted of a high-voltage pulse generator and a diode which could be filled with different gases at pressures from fractions to 760 Torr or be pumped off by a forevacuum pump. The construction of the cathode and the gas-filled diode, as well as the pressure and kind of the working gas, made it possible to vary electron beam parameters in a wide range. Note that we usually refer to the electron beam formed

Table 1. Parameters of subnanosecond and nanosecond accelerators

Accelerator and its mode	Maximum electron energy, keV	Beam current density j, A/cm^2	Current pulse duration at half-maximum $\tau_{0.5}$, ns	Pulse repetition frequency f, Hz
GIN-55-01 [60]	80	1.6	0.1	100
SLEP-150 [61]	250	10–230	0.1–0.6	1
SLEP-150M [62]	250	10–230	0.1–0.6	1
GIN-500 [63]	350	220	1.3	0.2
GIN-600 [52]	420	100	12	0.1
RADAN-220 [64] (mode 1)	200	75	0.18	1
RADAN-220 (mode 2)	210	1.1	0.1	1
RADAN-220 (mode 3)	200	120	0.3	1

in the gas-filled diode as SAEB (supershort avalanche electron beam) [65]. The electron beam for irradiation of samples under study was extracted from the accelerator through a thin anode foil. Figure 4 shows examples of waveforms of beam current pulses with an accelerator on the base of the SLEP-150M generator at different pressures of helium p in a gas-filled diode.

An important parameter in these investigations is the electron spectrum excited by the samples. The energy distribution of beam electrons was usually determined by attenuation of the SAEB current behind filters of aluminum foil with different thicknesses [65, 66]. To determine the energy of main groups of electrons, in addition to the filter method, a time-of-flight spectrometer was used. It consisted of a tube section with two diaphragms at end flanges [67]. The energy electron distributions for different accelerators with sleeve cathodes are presented in Fig. 5.

Since this survey is devoted to investigations of spectral and amplitude–time characteristics of VCR

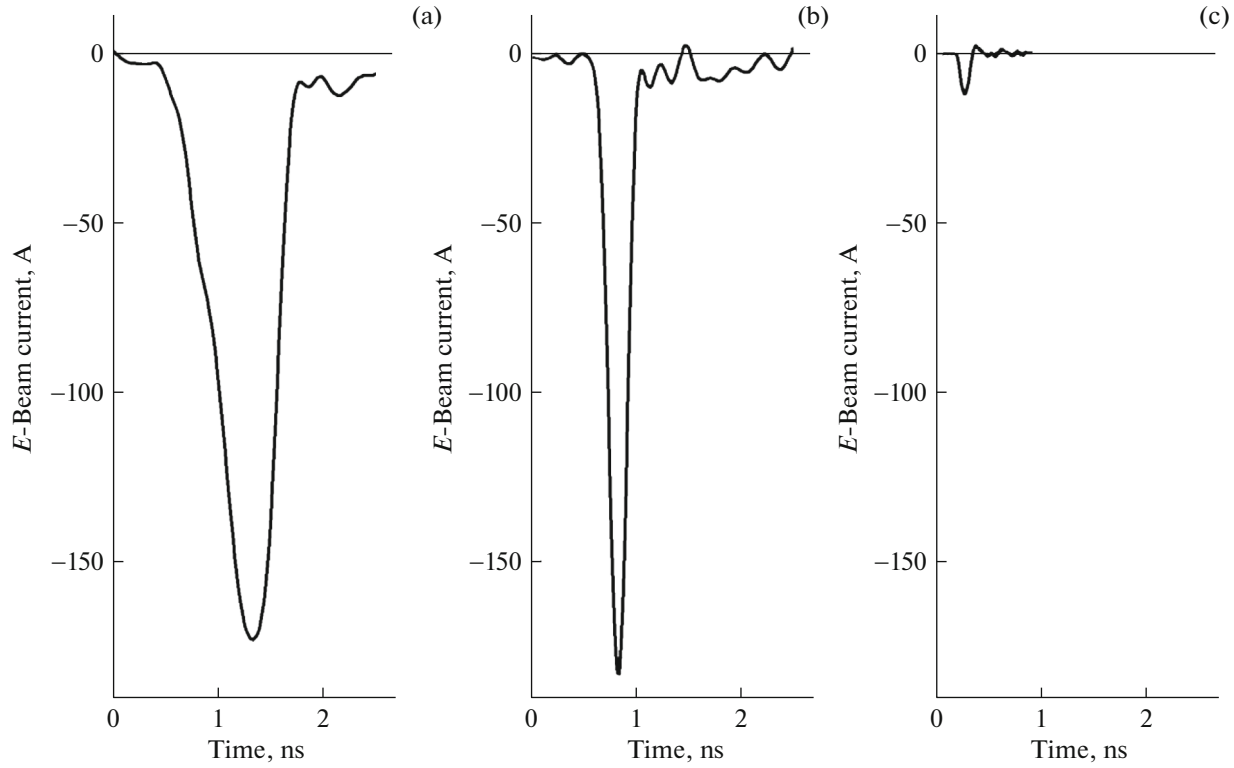

Fig. 4. Electron beam current pulses used for the action on samples at different gas pressures in the gas-filled diode behind the aluminum foil and diaphragm with a diameter of 1 cm. The gas pressure in the diode p = (a) 9, (b) 60, and (c) 760 Torr. A sleeve cathode and an interelectrode gap d = 14 mm.

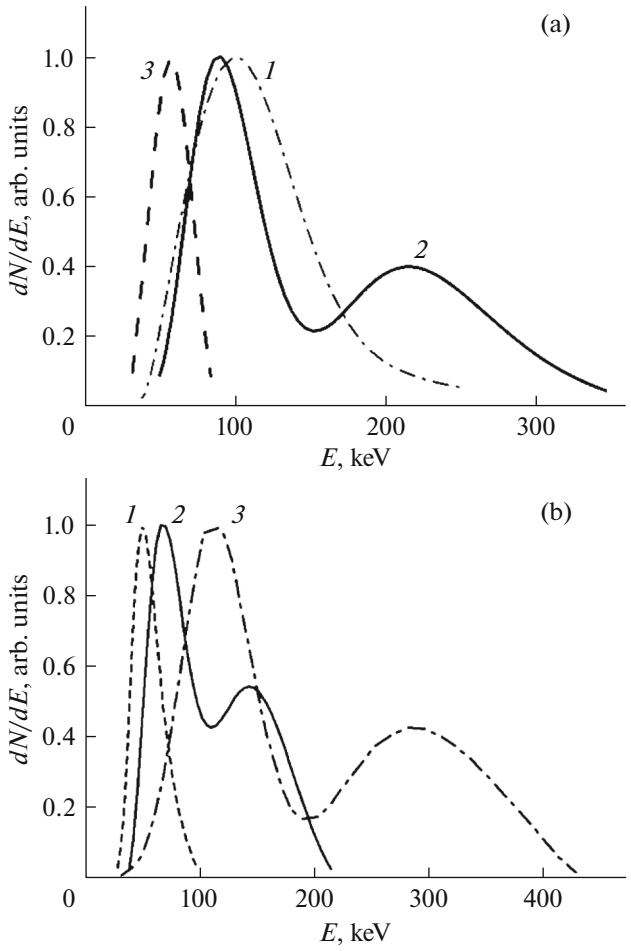

Fig. 5. (a) Energy distributions of beam electrons (*1*) for the accelerator based on SLEP-150M [51], as well as for the (*2*) first and (*3*) second pulses of the electron beam current of the accelerator on the base of GIN-500 at d = 11.5 mm and p ~ 0.8 Torr [63]. (b) Energy distributions of beam electrons for accelerators based on (*1*) GIN-55-01, (*2*) RADAN-220 [2], and (*3*) GIN-600 generators [40]. All distributions are normalized to unity.

and PCL, we describe in detail the construction of only one of the accelerators—GIN-500, which was designed in 2019 [63]. A detailed information about constructions of other accelerators and conditions for obtaining different regimes of the beam current can be found in [50–52, 60–67].

The schematic diagram of the construction of the GIN-500 accelerator consisting of a two-section high-voltage block and a gas-filled diode is shown in Fig. 6. In the first section of the accelerator, as in the RADAN-303 generator [68], a double forming line was used. However, instead of the gas-filled spark swich with an adjustable gap which was positioned in [68] between the middle and grounded coaxial electrodes, an R-49 industrial two-electrode spark swich connected with the inner electrode was used. The wave impedances of each of the two forming lines of the first section were equal to ~20 Ω. The impedance of the short transmission line following the double forming line was 50 Ω. On the grounded and middle electrodes in section I, magnetic circuits taken from a RADAN-220 generator [64] were positioned. After the short transmission line, the second section of the accelerator was mounted. It consisted of an inhomogeneous transmission line the wave impedance of which smoothly varied from 50 to 100 Ω. Using the second section allows one to increase the voltage pulse amplitude in a simple way. The diameter of the inner electrode at the input of the inhomogeneous line to the gas-filled diode was 8 mm and the inner diameter of the outer electrode of the coaxial line was equal to 102 mm. This provided comparatively high electric strength of the gas diode insulator.

The sleeve cathode with an inner diameter of 8 mm was manufactured of 100-μm-thick stainless steel foil. The interelectrode gap could vary from 2 to 13 mm. The beam current was extracted through a 40-μm-thick AlMg foil. The beam current was detected using a conical collector with a temporal resolution of up to 100 ps [69]. The voltage pulses at the output of the first and second sections were measured using capacitive dividers.

The double forming line was charged from the secondary winding of a pulsed power transformer which was positioned between two coaxial cylinders with built-in magnetic cores during the capacitor discharge through the primary winding (not shown in the figure). Then, on operation of the R-49 high-pressure spark swich, a nanosecond voltage pulse with an amplitude of ~190 kV was formed in section I. The pulse was delivered by the short transmission line and line with variable wave impedance to the sleeve cathode. This made it possible to obtain voltage pulses with a duration of 2.5 ns at half-maximum in the idle mode of ~500 kV. The gas pressure in the diode could vary from 0.1 to 760 Torr. In this accelerator, the gas diode was filled with air. As shown in [70], optimum pressures in the diode for obtaining maximum amplitudes of the beam current in helium, hydrogen, and nitrogen are different.

Oscillograms of the voltage and beam current pulses in the mode close to optimum for carrying out experiments on studying VCR parameters are shown in Fig. 7. The amplitude of the voltage pulse at the diode was not less than 350 kV and the current detected by the collector with the receiving part diameter of 15 mm was ~700 A. The density of the beam current behind the foil from the central area with a diameter of 3 mm was ~220 A/cm^2. Oscillograms of the voltage and beam current pulses in this mode consisted of two pulses. The duration of the first (main) pulse at half-maximum was $\tau_{0.5}$ ~ 1.3 ns. The second beam current pulse had a lesser amplitude. It appeared due to differences in the resistances of the generator and gas-filled diode, which increased with an increase

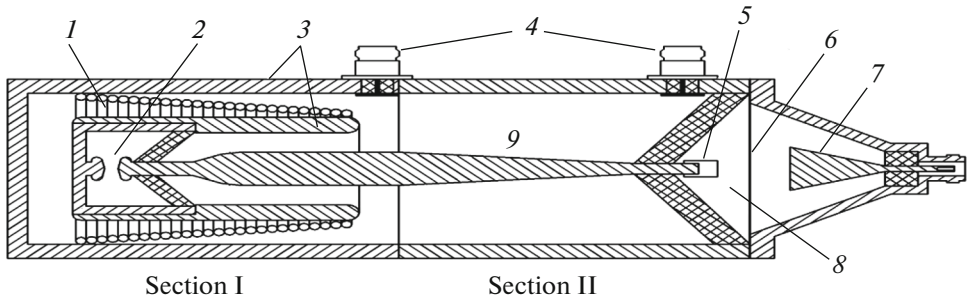

Fig. 6. Schematic diagram of the high-voltage accelerator block consisting of two sections and a gas-filled diode to which a conical collector is connected [63]. Both sections of the accelerator are filled with transformer oil. (*1*) Secondary winding, (*2*) spark gap, (*3*) coaxial line electrodes, (*4*) capacitive voltage dividers, (*5*) cathode, (*6*) anode foil, (*7*) collector, (*8*) diode, and (*9*) inhomogeneous transmission line.

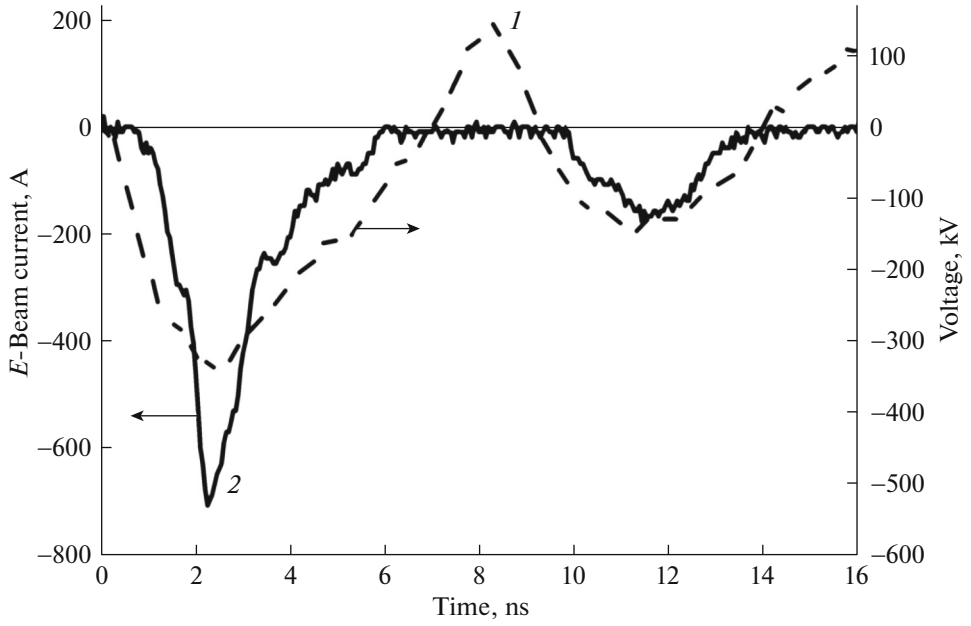

Fig. 7. Oscillograms of the (*1*) voltage pulse at the diode and (*2*) beam current behind the foil at the interelectrode gap $d = 11.5$ mm and air pressure in the diode $p \sim 0.8$ Torr [63].

in the diode resistance. For the first voltage pulse in the electron energy distribution, there were two groups in energy ranges of 50–150 and 180–350 keV. In the second pulse, under the same conditions, the electron energy did not exceed 100 keV and the distribution had a single maximum (Fig. 5a). The glow of quartz glass and sapphire samples under the action of an electron beam from the GIN-500 accelerator at a pulse duration at half-maximum of 1.3 ns is shown in Fig. 8. The created accelerator was used for exciting VCR in KU-1 quartz glass, leucosapphire, sapphire, synthetic type IIa diamond, yttrium oxide ceramics, and other materials. The results are presented in Section 4.

In PMMA damage experiments, it was more convenient to use values of electron beam energy density. The range of electron beam energy densities when varying the charging voltages of the GIN-600 generator was 0.01–0.4 J/cm^2. With the SLEP-150M generator, the maximal density of electron beam energy was ~0.01 J/cm^2, and minimal densities at which it was still possible to register SAEB oscillograms were three orders of magnitude lower. The variation was achieved by varying the pressure and gas kind in the diode.

In addition to the accelerators the parameters of which are presented in Table 1, the Tomsk Polytechnic University microtron [71] was used as an electron accelerator to study the dependence of the spectral composition of the quartz glass plate radiation on the angle of plate inclination to the direction of electron beam propagation. The study of spatial VCR characteristics extends the range of beam electron energies stated in the title of the survey. The use of the micro-

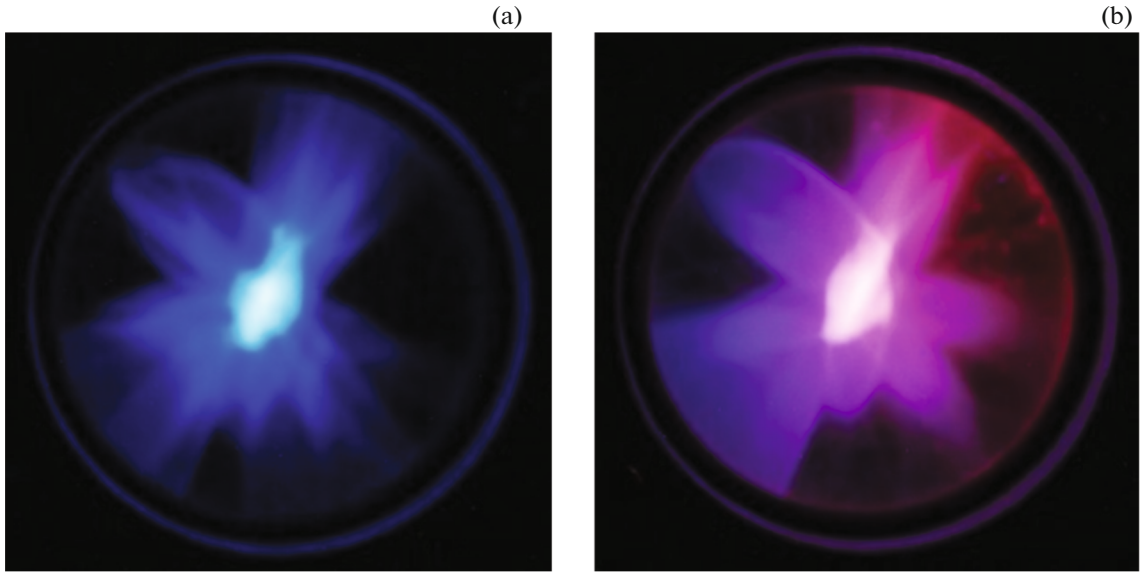

Fig. 8. Photographs of the glow of plates (radiators positioned perpendicularly to the direction of electron beam propagation) of (a) 8-mm-thick KU-1 quartz glass and (b) 5-mm-thick sapphire [42]. The photograph size is 65 × 65 mm. The glow of samples was photographed using a Sony α100 digital reflex camera GIN-500 accelerator.

tron is justified by the fact that it brings the beam electron energy closer to the upper limit of RE energies in tokamaks. The energy of beam electrons was equal to 6 MeV. The average beam current was 25 mA and the duration of the current pulse was 4 μs. The beam consisted of 10^4 bunches with the duration of ~10 ps of each bunch and delivered to the samples with a frequency of 3 Hz. The beam divergence after the extraction from the chamber corresponded to $\theta_e \sim 6°$. The duration of individual electron bunches and corresponding VCR pulses was shorter than the temporal resolution of the equipment used in the experiments.

For all accelerators except the GIN-600 based accelerator and the microtron, electrical signals from the capacitive dividers and collectors were delivered to an Agilent DSO X6004A digital oscilloscope (6 GHz, 20 S/ns) via 5D-FB PEEG (Radiolab) 1.2-m-long high-frequency cables. The signals were attenuated using 142-NM attenuators (Barth Electronics, 30 GHz). A Tektronix DPO 3034 digital oscilloscope (300 MHz, 5 S/ns) was used with the GIN-600 accelerator and microtron.

3.2. Schemes of the Experiments and Characteristics of Sample Materials

The luminescence of samples made of different materials under the action of an electron beam from the accelerators described above was studied on several test benches. Typical schemes of experiments on studying spectral and amplitude–time characteristics of the glow of different samples with excitation by an electron beam from the accelerators described in Table 1, as well as data on the transmission of the UFS filters and the sensitivity of the PD025 photodiode are presented in Fig. 9.

The samples were usually placed perpendicular to the direction of electron beam propagation or to the direction of excilamp emission. As was shown in [40], at electron energies of tens or hundreds of kiloelectronvolts, a considerable portion of VCR goes out perpendicularly to the sample surface due to multiple electron scattering and changes in the angle θ (Fig. 1b) between the electron motion direction and the VCR direction with a decrease in their energy in the deceleration process. This is also corroborated by photographs of the glow of KU-1 quartz glass and sapphire plates in Fig. 8.

The emission spectra of the samples, as well as their transmission spectra, were measured using an HR2000+ES spectrometer (with a spectral range of 190–1100 nm and a spectral resolution of 9 Å, Ocean Optics, Inc.) with known spectral sensitivity. The samples were typically mounted at a distance of 2.5 mm from the foil. Radiation was delivered to the spectrometer via a P600-1-SR light guide (with a spectral range of 200–1100 nm and a core diameter of 600 μm, Ocean Optics, Inc.). An AvaSpec-3648 fiber-optic spectrometer (with a range of 200–1100 nm and a spectral resolution of ~3 nm) was used when carrying out spectral measurements with excitation of sample luminescence by an electron beam from the GIN-600 accelerator [72].

At a high temporal resolution in the wavelength range of 200–700 nm, the amplitude–time characteristics of radiation were recorded using a Photek PD025

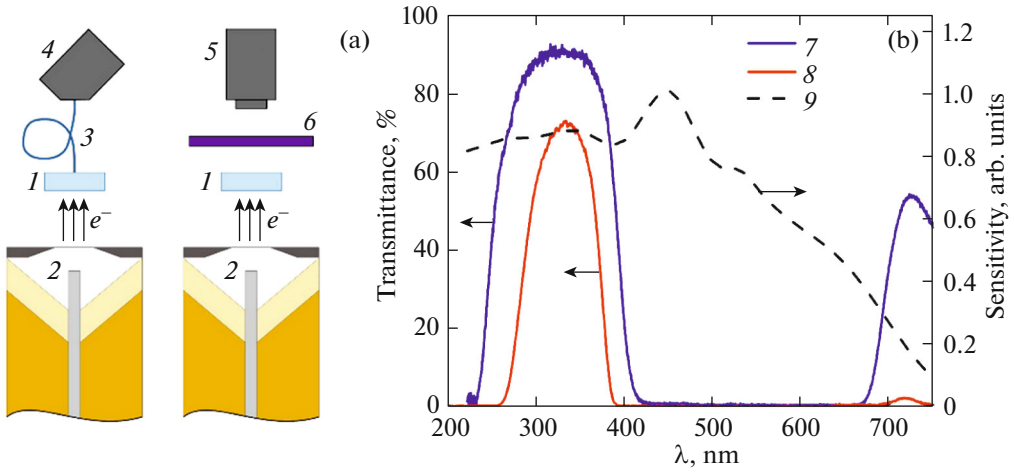

Fig. 9. (a) Schemes of systems for detection of radiation parameters with the use of a spectrometer and a photodiode and (b) data about transmission of UFS filters and sensitivity of the PD025 photodiode: (*1*) sample, (*2*) gas-filled or vacuum diode, (*3*) optical light guide, (*4*) spectrometer, (*5*) PD025 photodiode, (*6*) UFS-1 or UFS-2 optical filter, (*7*) transmission curve of the UFS-1 filter, (*8*) transmission curve of the UFS-2 filter, and (*9*) sensitivity curve of the PD025 photodiode.

photodiode (LNS20 cathode, the step response time ~80 ps) with installation of a UFS-1 (UFS-2) optical filter and without it (Fig. 9b). The shortwave boundary was determined by absorption of the samples or air; the longwave boundary, by the decrease in the photodiode sensitivity beginning from 500 nm. To reduce the influence of electromagnetic interference, the PD025 photodiode was placed in an aluminum beaker. In all experiments, signals from the PD025 photodiode were recorded using an Agilent DSO-X6004A digital oscilloscope (6 GHz, 20 S/ns).

The amplitude-time characteristics of radiation at a specific wavelength were recorded using an MDR-23 diffraction monochromator (grating with 1200 grooves/mm, inverse linear dispersion is 1.3 nm/mm, and the width of the input and output slit is 400 μm) and FEU-97 photomultiplier (the working wavelength range of 250–650 nm and the step response time is ~7 ns) [73], or FEU-84 photomultiplier (the working wavelength range 300–800 nm, step response time ~5 ns) [40], or H7732-10 Hamamatsu photomultiplier (wavelength range is 185–900 nm, the sensitivity range is 10^3–10^7, and the step response time is 2.2 ns) with known spectral sensitivity [72], and a Tektronix DPO 3034 (300 MHz) or Tektronix TDS3054B (500 GHz, 5 S/ns) digital oscilloscope connected to a computer. The samples were placed perpendicularly or at a 45° angle to the monochromator axis; the radiation was focused by a lens to the monochromator slit.

In [72], two methods for recording the luminescence spectra of Ga_2O_3 crystals were used: "point-by-point spectrum" and "spectrum per pulse." The first method allowed time-resolved registration of luminescence spectra using a pulse spectrometer based on the MDR-23 diffraction monochromator, FEU-97 photomultiplier, and a Tektronix DPO 3034 oscilloscope connected to a computer. The temporal resolution of the whole system for recording spectral characteristics of sample luminescence was ~15 ns. In the second method, the luminescence spectra (total per excitation pulse, without temporal resolution) were recorded using an AvaSpec-3648 fiber-optic spectrometer.

Characteristics of the samples under study are presented in Tables 2 and 3. For crystals with birefringence, values of the refractive index of the ordinary ray are given. For CdS and Ga_2O_3 crystals, as well as for yttrium oxide ceramics, it was not possible to find exact data on the longwave boundary of the transparency area; for this reason, Table 3 shows the longwave boundary of the working range of the HR2000+ES spectrometer (~1 μm). However, as in the case of diamond, the exact value of the longwave boundary of the transparency area is not important for the further presentation.

Gallium(III) oxide has several modifications; the β-phase is treated as the most stable one. In experiments [72, 74], two samples of β-Ga_2O_3 (nos. 1 and 2) were used: a Sn-doped semiconductor (no. 1) and Fe-doped semi-insulator (nos. 1 and 2). Characteristics of monocrystalline β-Ga_2O_3 plates grown by Stepanov's method (the EFG-method, Tamura Corp. [75]) were studied. In [76], a sample of yttrium oxide (Y_2O_3) ceramics with addition of 0.05 mole fraction of ZrO_2 was used in the experiments. The ceramics samples were manufactured in the Institute of Electrophysics, Ural Branch, Russian Academy of Sciences, from a nanosized powder obtained by laser synthesis [77].

Values of the refractive indices n_D for different crystals were taken from the refractive index database [78].

Table 2. Characteristics of most promising samples

Sample parameters: Type of the sample material (sample notation)	Transmission band, μm	Refractive index of the ray (n_D)	Electron threshold energy (E_{th}), keV
Diamond, type IIa, synthetic, CVD (C5)	0.225–(>5)	2.42	50
Diamond, type IIa, synthetic, CVD (C6)	0.225–(>5)	2.42	50
Diamond, type IIa, natural (C4)	0.225–(>5)	2.42	50
Sapphire, Al_2O_3	0.18–2.3	~1.77	108
Leucosapphire, Al_2O_3	0.18–2.3	~1.77	108
PMMA	0.35–2.0	1.49	178
KU-1 and GE014 quartz glass, SiO_2	0.16–3	1.46	190

The longwave boundary of the transmission band of diamonds is shown conventionally (more than 5 μm). Its exact value does not matter for the further presentation because it lies in the IR spectral range while the investigated spectral range of VCR excitation is bounded by the UV and visible ranges.

Table 3. Sample characteristics

Sample parameters: Type of the sample material (sample notation)	Transmission band, μm	Refractive index of the ray (n_D)	Electron threshold energy (E_{th}), keV
Diamond, type IIa, natural (C4)	0.225–(>5)	2.42	50
Diamond, type IIa, synthetic, HPHT (CN3)	0.225–(>5)	2.42	50
ZnSe	0.475–20	2.4	51
CdS	0.52–1	2.4	51
ZnS	0.37–13.5	2.2	63
ZrO_2	0.35–7	2.16	65
Ga_2O_3	0.26–1	1.97	82
Yttrium oxide ceramics	0.25–1	1.93	86
CsI	0.3–35	1.74	113
$CaCO_3$	0.25–2.5	1.57	152
CaF_2	0.125–12	1.434	202
MgF_2	0.11–7.5	1.38	230

The data were taken from [34]. The longwave boundary of the transmission band of diamonds is shown conventionally (more than 5 μm). Its exact value does not matter for the further presentation because it lies in the IR spectral range while the investigated spectral range of VCR excitation is bounded by the UV and visible ranges.

The short-wavelength boundary of the transparency area for a number of crystals was determined using the HR2000+ES spectrometer with sensitivity in the wavelength range of 190–1100 nm; the data on the longwave boundary of the transparency area for some crystals were taken from different sources [79, 80]. The same sources were used to take data on the shortwave boundary of the transparency area for crystals for which it lay in the region shorter than 190 nm.

The studies on the determination of spatial characteristics of the emission of quartz glass plates using the microtron [41] were carried out on the facility the scheme of which is shown in Fig. 10. Plane-parallel plates made of GE-014 and KU-1 quartz glass were used for the experiments. These types of quartz glass were chosen because of their low PCL intensity and low absorption in the wavelength range of 200–800 nm. The main experiments were carried out with the GE-014 quartz glass plate which had the smallest thickness. For the abovementioned thickness, the multiple scattering angle was $\theta_{ms} \sim 23°$. The emission spectra were registered by an Ocean Optics HR2000+ spectrometer, which was remote from the electron beam trajectory and was protected from their penetration, as well as the lead screen from X-ray radiation. Note that the X-ray radiation had the greatest intensity near the accelerator and near the irradiated plate and the electron beam trajectory. The light radiation from

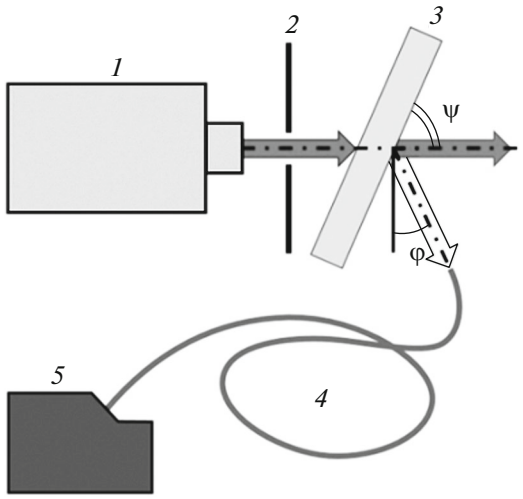

Fig. 10. Scheme of the experimental setup [41]: (*1*) microtron, (*2*) diaphragm, (*3*) quartz glass plate, (*4*) light guide, and (*5*) spectrometer.

the samples to the spectrometer was fed by a 2-m-long light guide which was also protected from X-rays and direct penetration of the electron beam.

In addition to electron beams from different accelerators, excilamps with radiation at 172, 206, 222, 282, and 308 nm were used to affect the samples [81–83]. The main experiments were carried out with KrCl-excilamps (the emission wavelength $\lambda = 222$ nm). The average radiation power density at the pulse repetition frequency $f = 43$ kHz was 7 mW/cm^2; the duration of the radiation pulse at half-maximum was $\tau_{0.5} \sim 200$ ns. The spectral and amplitude–time characteristics of the sample glow were registered on the same equipment as upon excitation by an electron beam.

4. VCR AND PCL OBSERVED IN DIFFERENT MATERIALS UPON EXCITATION BY AN ELECTRON BEAM

4.1. Spectral and Amplitude–Time Characteristics of VCR and PCL

A large number of studies (e.g., monographs [31, 37]) have been devoted to the study of PCL arising during irradiation of different materials with electron beams with energies of tens or hundreds of kiloelectronvolts. In some publications, a detailed analysis of the spectral composition of luminescence of samples was performed. However, at electron energies of hundreds of keV, as is shown in this section, the Vavilov–Cherenkov radiation also occurs. Below are the results of studies that were aimed at finding materials (dielectrics and semiconductors) and conditions for their excitation, suitable for detection of VCR arising when samples are irradiated with electron beams the electron energies of which lie in the range of tens or hundreds of kiloelectronvolts. The samples used had different shapes and sizes, but their thickness was sufficient for the beam electrons to be completely absorbed in the sample.

In [34, 35, 82, 83], SAEBs and UV radiation acted on materials with different refractive indices. The RADAN-220 and GIN-55-01 accelerators and a KrCl excilamp were used. Schematics of the experiments are shown in Fig. 9a. The samples chosen were natural and synthetic type IIa diamonds, cesium iodide (CsI), zinc sulfide (ZnS), leucosapphire (Al_2O_3), fluorite (CaF_2), zirconium dioxide (ZrO_2), gallium(III) oxide (Ga_2O_3), calcite ($CaCO_3$), cadmium sulfide (CdS), and zinc selenide (ZnSe). Diamond, ZnSe, CdS, ZnS, and ZrO_2 had the highest refractive indices. However, CdS and ZnSe samples are not suitable for the creation of Cherenkov sensors because they have appreciable transmittance only in the longwave speattral range (>500 nm). The CaF_2 and Al_2O_3 (leucosapphire) samples transmit light well not only in the UV spectral range but also in the VUV range; however, they have small refractive indices. The refractive indices of CsI and $CaCO_3$ are also relatively small.

The PCL spectra under the action of SAEB were detected in all investigated samples. On the background of cathodoluminescence, VCR was not registered using standard spectrometers in any of the samples due to its low intensity. This agrees with the data of works [31, 37, 84]. The obtained spectra for a number of samples with different refractive and transmittance indices are shown in Figs. 11 and 12.

The same figures present transmission spectra and, for a number of samples, their photoluminescence bands. Special attention in these studies was paid to samples of natural and synthetic type IIa diamonds because diamonds have a number of unique physical characteristics and are used as radiators of Cherenkov detectors, allowing one to determine the presence of electron fluxes beginning from energies of ~50 keV [16–18, 29, 85].

In the PCL spectra of natural diamond (Fig. 11a), in the region of 330–650 nm under electron beam excitation both from the RADAN-220 accelerator (in modes 1 and 2) and from GIN-55-01, one can see the well-known superposition of the structureless A-band and the electron-vibrational system (EVS) N3 [38, 86]. The A-band at 430–460 nm is caused by intrinsic defects—sp^2-hybridized carbon bonds [87]. The N3 EVS centers are complex defects involving three substituted nitrogen atoms in neighboring lattice nodes in the ⟨111⟩ plane associated with a common vacancy—N_3V defects [88]. The zero phonon line (ZPL) of N3 ECS is observed at 415 nm; its main phonon repetitions are at 428, 439, and 452 nm. In the region of 225–310 nm which falls within the transmission range of the used diamond crystals and in which VCR should be observed, the emission on the spectrograms had a low intensity and was not reliably detected.

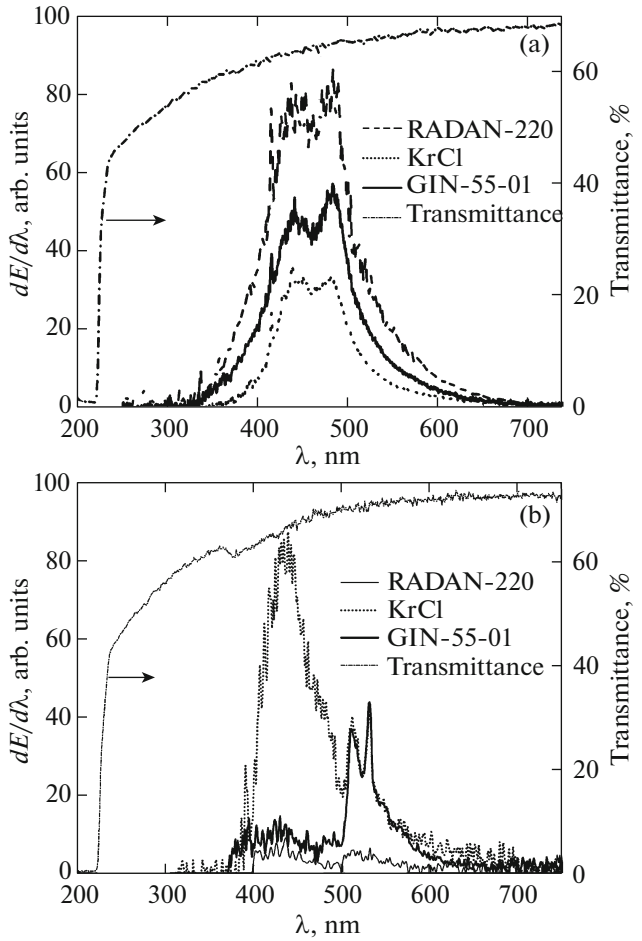

Fig. 11. Transmission and radiation spectra of (a) natural and (b) synthetic diamond upon excitation by SAEB from the GIN-55-01 generator and from the RADAN-220 generator in mode 1, as well as upon excitation by a KrCl-excilamp [34].

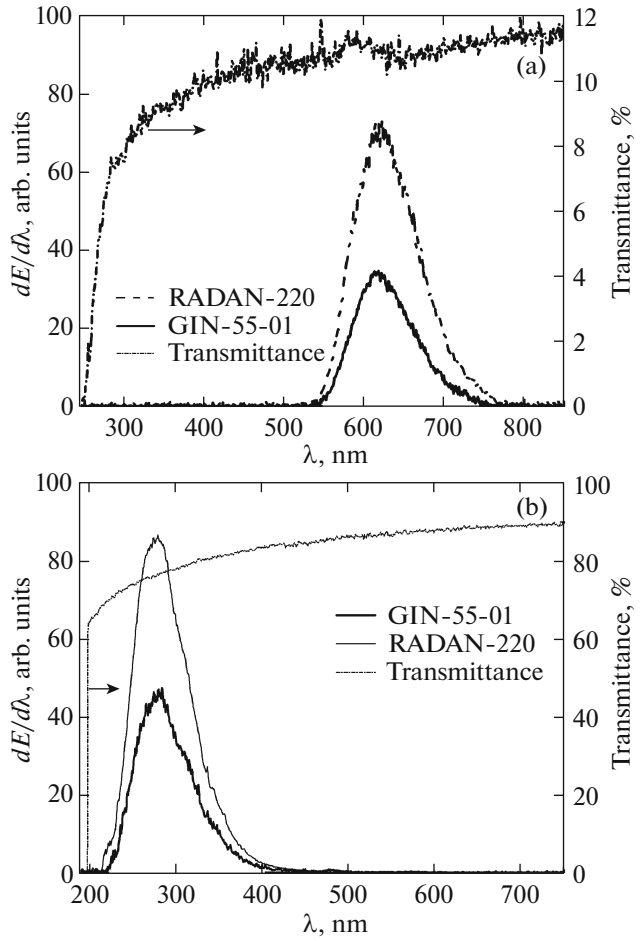

Fig. 12. Transmission and radiation spectra of (a) $CaCO_3$ and (b) CaF_2 upon excitation by SAEB from the GIN-55-01 generator and from the RADAN-220 generator in mode 1 [34].

In the PCL spectra of synthetic diamond (Fig. 11b), the radiation intensity in the region of 350–650 nm decreased, the distribution of the radiation energy over the spectrum in this region changed, and the dependence of the spectrum on the excitation mode became apparent. The strongest decrease of the detected radiation intensity in the region of 330–650 nm was obtained at a low pulse repetition rate (1 Hz). Moreover, during the RADAN-220 operation in mode 2, it was not possible to detect the synthetic diamond emission spectrum due to the decrease of the SAEB current density by more than one order of magnitude. Upon excitation in the pulse-periodic mode with a frequency of 60 Hz, the decrease in the radiation intensity in the region of 330–650 nm was less than in the single pulse mode. In addition, using the GIN-55-01 accelerator changed the distribution of optical radiation energy over the spectrum. In addition to the A-band at 430–440 nm, EVS of 389 nm and 3H were observed in the PCL luminescence spectrum [31]. The 389 nm electron-vibrational system is named after the spectral position of the ZPL; its phonon repetitions are observed at 400, 410, and 420 nm. The zero phonon line of EVS 3H at 503 nm is characterized by low intensity at room temperature; its main phonon repetitions are observed at 510 and 530 nm. At this time, models of 389 nm and 3H EVS centers have not yet been proposed to describe all the observed data; however, one assert that the EVS data are due to interstitial atoms, i.e., radiative defects [31]. In the region of 225–350 nm, the emission in the spectrograms was weak and was not reliably detected, as during the opration of the RADAN-220 accelerator in mode 1. Correspondingly, with an increase in the repetition frequency of the SAEB current pulses, the radiation intensity of synthetic diamond in the region of 330–650 nm increases, which may be caused by the accumulation of radiation defects that do not have time to relax in the pauses between the excitation pulses.

Upon excitation by pulses of UV radiation ($\lambda \sim$ 222 nm) with a duration of ~ 200 ns from the KrCl-excilamp, which followed at a frequency of 43 kHz and provided an average power density of 7 mW/cm^2 on the samples, EVS of 389 nm and 3H (500–540 nm) were also observed. The intensity of the A-band in the region of 400–500 nm increased significantly. It follows from these results that irradiation of diamonds with shortwave UV radiation increases the intensity of diamond emission in the region of 350–650 nm. Correspondingly, if the VCR intensity is sufficient, it can contribute to the integral luminescence of diamond due to photoluminescence.

In natural and synthetic diamonds (Fig. 11), in $CaCO_3$ (Fig. 12a), as well as in ZnS and Ga_2O_3, there is a rather large spectral range between the absorption band edge and the luminescence band edge in which there is no emission visible on spectrograms at the noise level. In CsI crystals, the shortwave edges of the absorption and cathodoluminescence bands almost coincide, which complicates VCR detection in this range. In CaF_2 (Fig. 12b), despite the fact that the shortwave edge of the absorption band lies in the VUV region of the spectrum, the luminescence band edge reaches 225 nm, and in the region shorter than 225 nm the absorption of the quartz light guides increases significantly. In the region shorter than 200 nm, in addition, the absorption of air increases sharply. Thus, based on the obtained emission spectra, one could expect VCR detection when using more sensitive measurement methods, first of all, in synthetic diamond.

Upon excitation with a KrCl-excilamp, photoluminescence, as noted above, was detected in natural and synthetic diamonds, as well as in CsI, ZnS, ZrO_2, and Ga_2O_3. In leucosapphire and CaF_2, due to their low absorption in the region of 200–250 nm, photoluminescence was not detected. Due to strong absorption in the spectral range shorter than 500 nm, photoluminescence was not detected in CdS and ZnSe; in $CaCO_3$, due to the irregular shape of the samples under study. It follows from experiments with the KrCl-excilamp that shortwave radiation makes a contribution to cathodoluminescence bands of most of the studied samples and that the cathodoluminescence and photoluminescence bands are similar. Therefore, VCR the intensity of which increases with a decrease in the wavelength can make a contribution to emission of samples due to photoluminescence upon excitation of VCR in the spectral range with strong absorption in the sample.

The amplitude-time characteristics were taken with the Photek PD025 photodiode, which had a subnanosecond temporal resolution but low sensitivity, and with the Hamamatsu H7732-10 PMT, which was installed behind the monochromator. In the second case, due to the high sensitivity of the PMT, measurements of the amplitude–time characteristics of radiation pulses were performed at certain wavelengths even at low radiation intensities at these wavelengths. However, the temporal resolution in this case was worse than that of the PD025 photodiode and was determined mainly by the decay time of the pulse response (10 ns at the level of 0.9–0.1). Figure 13 presents oscillograms of synthetic diamond cathodoluminescence upon SAEB excitation with a duration of ~100 ps at half-maximum. The duration of the radiation pulse was about 2 ns at the half-maximum as its front was of 1 ns. Note the presence of a bend at the front of the emission pulse, which may be related to the detection of VCR during the beam current pulse. In this case, however, cathodoluminescence is mainly detected. The time resolution of the detection system under these conditions was not worse than 0.3 ns.

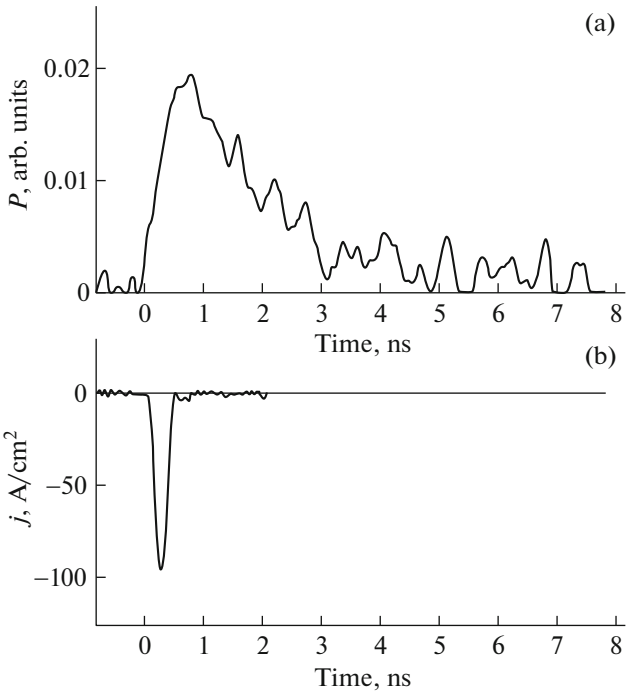

Fig. 13. Oscillograms of (a) cathodoluminescence of synthetic diamond and (b) beam current density [84].

As noted above, the area between the shortwave edge of the transmission band of the materials and the shortwave boundary of cathodoluminescence is the most suitable for VCR detection. When using a PMT and a monochromator upon excitation from the RADAN-220 accelerator, VCR was detected in this region in diamond (natural and synthetic), ZnS, ZrO_2, Ga_2O_3, leucosapphire, and even in CsI. The sensitivity of the used PMT turned out to be sufficient for reliable VCR detection in these samples. To detect VCR in CaF_2 and $CaCO_3$, an electron beam with a higher energy (>200 keV) should be used. CdS and ZnSe samples are unsuitable for VCR sensors due to their large absorption in the spectral region of <500 nm.

Mentioning CdS and ZnSe, we also mention Nasibov's works summarized in the survey [89]. In those works, it was reported about obtaining of laser radiation in the semiconductor compounds CdS_xSe_{1-x} and ZnSe, as well as in other crystals. It was shown that the RE beam current density can reach a value sufficient for the appearance of stimulated emission even at atmospheric pressure.

Studies using a monochromator and a PMT showed that, in the region of 225–310 nm for natural diamond and in the region of 225–350 nm for synthetic diamond, the spectral energy density increases with a decrease in the wavelength [34]. In these regions, one can expect exciton band luminescence with a maximum at 235 nm; however, the luminescence decay time of the exciton band in type IIa diamond is tens of nanoseconds [90]. The recorded duration of the emission pulses of diamond samples in these regions does not change and corresponds to the time resolution of the H7732-10 Hamamatsu PMT, i.e., it is several times shorter than the exciton luminescence decay time. Also, the minimal delay of the emission pulses of the diamond samples with respect to the voltage pulse front is observed. Correspondingly, the detected optical emission in this region can be referred to VCR. Beginning from a wavelength of 310 nm for natural diamond and 350 nm for synthetic diamond, an increase in power and in the duration of emission pulses by several times is observed as the wavelength increases. In addition, in this wavelength range there appears a delay of the radiation pulses relative to the radiation pulses associated with VCR; it increases smoothly up to 4–5 ns.

Similar small delays and increased pulse duration of radiation during detection in the cathodoluminescence region relative to radiation in the region between the shortwave edge of absorption and the shortwave boundary of cathodoluminescence when using a high-sensitivity PMT and a monochromator were obtained for samples of ZnS, ZrO_2, Ga_2O_3, Al_2O_3, and CsI. Correspondingly, VCR was also detected in these materials.

In [72, 74], an in-depth study of luminescence of crystal samples of gallium(III) oxide was carried out to determine suitability of Ga_2O_3 crystals for VCR detection when creating RE sensors for tokamak-type facilities. Ga_2O_3 crystals were excited with an electron beam using RADAN-220 accelerators in modes 1 and 2, as well as GIN-55-01. The luminescence spectra of Ga_2O_3 crystals excited by an electron beam and UV radiation significantly depend on the type of doping. The cathodoluminescence band in the region of 300–450 nm has the greatest intensity upon electron beam excitation. This band is also detected when a Sn-doped crystal is excited by UV radiation of a KrCl excilamp. In a Fe-doped crystal, a second band appears in the 650–900 nm region for both excitation methods. However, in this crystal, the photoluminescence in the range of 300–450 nm was weak and was not detected on the background of noises. Note that the band intensity in this crystal in the region of 300–450 nm was significantly less than in the Sn-doped crystal. This may be due to the fact that the concentration of free charge carriers with the Fe doping impurity was significantly lower than with Sn. No VCR was detected using the spectrometer on the base of the GIN-55-01 and RADAN-220 accelerators.

The Vavilov–Cherenkov radiation in the region of 250–300 nm was detected on the RADAN-220 accelerator only using a monochromator and a PMT. This could be done both in mode 1 at a beam current density of 75 A/cm^2 and in mode 2 at a beam current density of 1.1 A/cm^2. The radiation at a wavelength of 265 nm has the minimal delay with respect to the voltage pulse, and its duration and shape correspond to the pulse response of the photomultiplier tube used. When the radiation was detected in the PCL region, the amplitude of the radiation pulses and the duration of the pulses from the PMT increased, which corresponded to the observed radiation spectra. Thus, Ga_2O_3 crystals can be used for detection of REs with energies higher than 82 keV using VCR. However, PCL is significantly more sensitive to excitation by electron beams at wavelengths >300 nm, especially in Sn-doped crystals. Moreover, cathodoluminescence is also observed at electron energies lower than 82 keV.

Using a photodiode with a high temporal resolution for the radiation detection made it possible to detect integral radiation pulses in the range of 250–700 nm, as well as VCR pulses in the range of 250–300 nm, on the RADAN-220 accelerator (operating in mode 1) [34, 74]. In this region, the studied Ga_2O_3 crystals were still transparent, and the cathodoluminescence had a low intensity.

A series of experiments [40, 72, 73] on studying the luminescence of diamond, leucosapphire, quartz glass and MgF_2 samples were carried out on the GIN-600 accelerator in which the electron energy reached 400 keV (Fig. 5b). Schematics of the experiments are shown in Fig. 9a. In these measurements, excitation was implemented at a beam current density of ~100 A/cm^2. The maximum electron energy was twice the energy of electrons of the RADAN-220 accelerator. Figure 14 shows spectra of radiation and light transmission of natural and synthetic diamonds obtained by different methods. It is well known that emission spectra of diamonds depend on the method of their production, as well as on the composition of impurities in them [31, 37]. For this reason, the obtained emission spectra differ significantly, except for the spectra of high-purity diamonds (C5 and C6, Table 2) obtained by gas-chemical deposition. For C5 and C6 samples, an increase of the radiation intensity in the spectral region of 250–400 nm was detected with a decrease of the radiation wavelength, which is one of the main features of VCR. For natural diamond

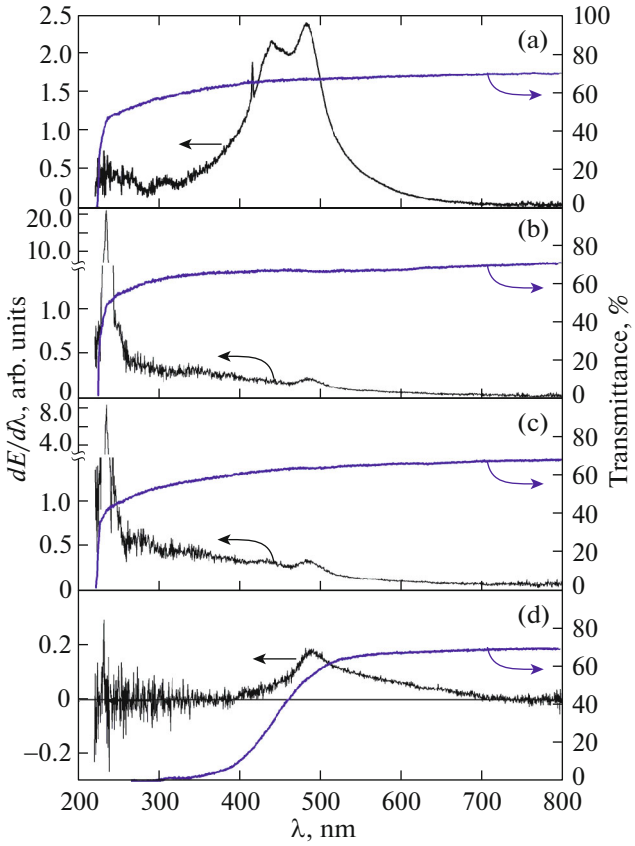

Fig. 14. Radiation and transmission spectra of four diamond samples obtained by different ways: (a) C4, (b) C5, (c) C6, and (d) CN3 [40]. GIN-600 accelerator.

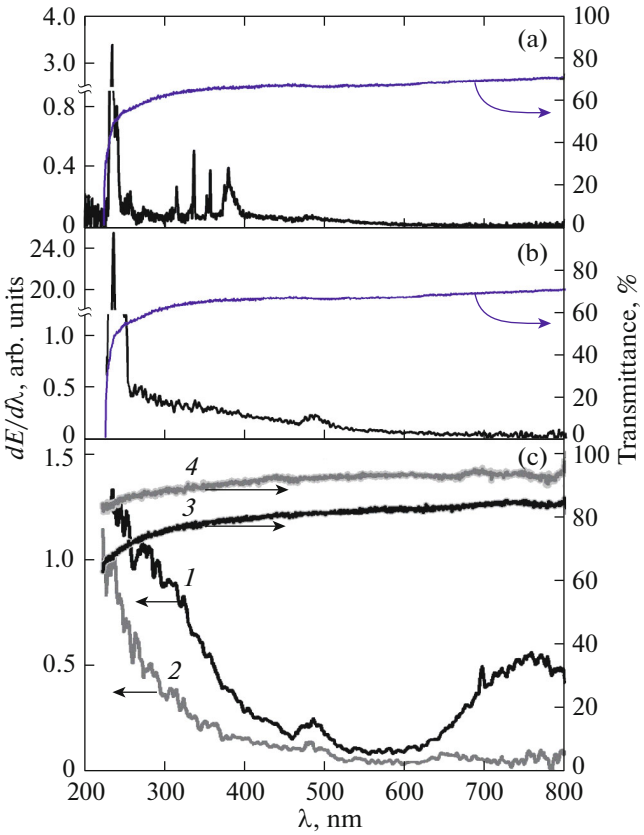

Fig. 15. Radiation and transmission spectra of the C5 diamond sample upon excitation by an electron beam from the (a) RADAN-220 accelerator and (b) GIN-600 accelerator; (c) radiation and transmission spectra of (*1*, *3*) leucosapphire and (*2*, *4*) KU-1 quartz glass upon excitation by an electron beam on the GIN-600 accelerator [40].

C4, an essential contribution to the radiation in this region was made by cathodoluminescence; for diamond CN3, the emission spectrum was influenced by absorption. The shapes of the absorption curve for the C4, C5, and C6 crystals did not differ significantly, but the high intensity of cathodoluminescence in the C4 crystal did not allow one to reliably identify VCR by the spectrometer. Strong absorption in the CN3 crystal (in view of the presence of dispersively distributed nitrogen atoms substituting the lattice atoms) beginning from 500 nm explains the absence of VCR in its spectrum.

In addition to VCR, a band with high spectral energy density in the region of 220–350 nm was detected using a spectrometer on the GIN-600 accelerator, as well as on the RADAN-220 accelerators with increasing beam current density and pulse duration for samples C5 and C6. This band was absent in natural diamond (sample C4) and in sample CN3. As shown by the cathodoluminescence studies in [91], the band of 220–350 nm refers to the emission of excitons in diamond. The intensity of this band increases with a decrease in temperature.

As follows from results of [40], VCR was confidently recorded on the facility GIN-600 accelerator. The facility had higher electron energies and beam current duration compared to those used in [34]. The increase in the beam current density from 75 to 120 A/cm^2 and half-maximum pulse duration from 180 to 300 ps on the facility with the RADAN-220 accelerator also made it possible to detect an increase in the radiation intensity in the region of 240–300 nm with a decrease of the radiation wavelength using a standard spectrometer. This, as already noted, indicates VCR detection in this region. In addition, an exciton band in the region of 220–350 nm with a maximum at the wavelength of 235 nm was also registered on this facility at the electron energy of up to 200 keV. For comparison, Fig. 15 shows emission spectra obtained on the GIN-600 and RADAN-220 facilities for the C5 diamond crystal. In addition to VCR and PCL, at a beam current pulse duration of 0.3 ns, the second positive nitrogen system bands are clearly seen on the emission spectrum in the region of 300–400 nm (Fig. 15a). The line with a wavelength of

337.1 nm had the highest intensity. However, these bands were absent at a pulse duration of 12 ns and a beam current density of 100 A/cm^2. Moreover, the nitrogen bands in the emission spectrum during excitation of diamond were absent both in the first series of experiments (Fig. 14b) and in the second series (Fig. 15b). One can assume that the radiation intensity of the second positive nitrogen system in the second case decreases strongly due to quenching of the excited levels of the nitrogen molecule by plasma electrons. As a result, the spectral energy density of the emission of nitrogen bands registered by the spectrometer turns out to be lower on the GIN-600 facility than the spectral energy density of VCR.

Thus, it was possible to register spectra of diamond emission using a spectrometer on two facilities where the increase in the radiation energy density in the region of 250–340 nm was noticeable. These spectra also exhibited a narrow band with a maximum at 235 nm with high spectral density of radiation energy; it was absent when using the RADAN-220 facility with a lower beam current density.

The emission spectra were also recorded using a spectrometer in leucosapphire and KU-1 quartz glass (Fig. 15c) [40]. These materials were chosen for the studies because they have a relatively low intensity of cathodoluminescence in the UV region of the spectrum, and the edge of the fundamental absorption is in the VUV region. As seen in Fig. 15c, both samples have a band in the wavelength region of 220–450 nm. Its intensity increases with a decrease in the wavelength. This increase in the intensity can be explained only by the presence of VCR. For an additional verification of this conclusion, the amplitude–time characteristics of the emission in diamond (sample C6), leucosapphire, and KU-1 quartz glass were measured.

An important feature of VCR is the correspondence of its duration to the duration of the electron beam. The amplitude–time characteristics of the radiation were investigated on facilities with the GIN-600 and RADAN-220 accelerators using a PD025 photodiode (Fig. 9b). The emission pulses were compared with the beam current oscillograms. The radiation pulses were detected behind a UFS-1 light filter which transmitted radiation into the spectral region where VCR (230–400 nm) was observed. The transmission curve of the light filter is shown in Fig. 9c. In the region of the second transmission band of the UFS-1 light filter (>670 nm), the photodiode sensitivity decreases significantly, and the light filter transmission does not exceed 55% even at the band maximum at a wavelength of 720 nm.

For diamond (sample C5) the shape of the radiation pulse approximately corresponds to that of the beam current up to its maximum. Further, an increase in the radiation intensity and pulse duration is observed both with the use of the UFS-1 filter and without it. It follows that the cathodoluminescence, along with the Vavilov–Cherenkov radiation, makes a contribution to the detected radiation. However, the contribution of the exciton emission band in the range of 220–350 nm to the signal detected by the photodetector during the first 20 ns is relatively small due to the long duration of the radiation pulse corresponding to this band (~80 ns at half-maximum) upon excitation from the GIN-600 accelerator. The radiation intensity decreased rapidly after the 12th nanosecond. The duration of the exciton band pulse was determined using a monochromator and a PMT.

For sapphire and leucosapphire, the best agreement between oscillograms of the beam current and radiation was observed. The contribution of sapphire PCL in the longwave range of the spectrum (>650 nm) to the detected signal was insignificant. For the KU-1 quartz glass, the radiation pulses were approximately equal in total duration to the duration of the beam current pulses but consisted of three consecutive peaks. These peaks appeared due to voltage fluctuations at the vacuum diode, which led to changes in the beam current density and electron energy. At the same time, three peaks were observed both with the filter and without it. The main contribution to these pulses is made by VCR; however, because of the small refractive index, half of the beam electrons did not have enough energy to exceed the threshold (E_{th} = 190 keV).

This conclusion is corroborated by experiments on the facility with the GIN-500 accelerator [42]. The experiments were carried out with synthetic diamond C5, sapphire, and KU quartz glass (Table 2). The investigatioins show that the emission spectra of all samples exhibit a band in the region of 220–400 nm and its intensity increases with a decrease in the wavelength. This radiation corresponds to the calculated spectrum and relates to VCR. The VCR spectra were calculated using the well-known formula (5) presented in Section 2 for the spectral power density of VCR. The emission and transmission spectra of synthetic diamond are presented in Fig. 16a. Several bands can be distinguished in the emission spectrum of high-purity synthetic diamond. The spectral energy density of radiation $dE/d\lambda$ in the region of 260–450 nm increases with a decrease in the wavelength, which is typical for VCR. At the same time, a narrow and intense band in the shortwave range of 230–240 nm is noticeably seen in the spectrum. Since the emission spectrum is a time-integrated characteristic, high values of $dE/d\lambda$ in the range of 230–240 nm can be also determined by the duration of diamond emission in this spectral range. The emission of this narrow band with a maximum at a wavelength of 235 nm, as in [73, 82], is caused by radiative recombination of free excitons [31]. In the region of 400–600 nm, the diamond cathodoluminescence bands are observed; they were also observed in [34] for synthetic diamond.

The emission and transmission spectra of KU-1 quartz glass are shown in Fig. 16b. In quartz glass, the

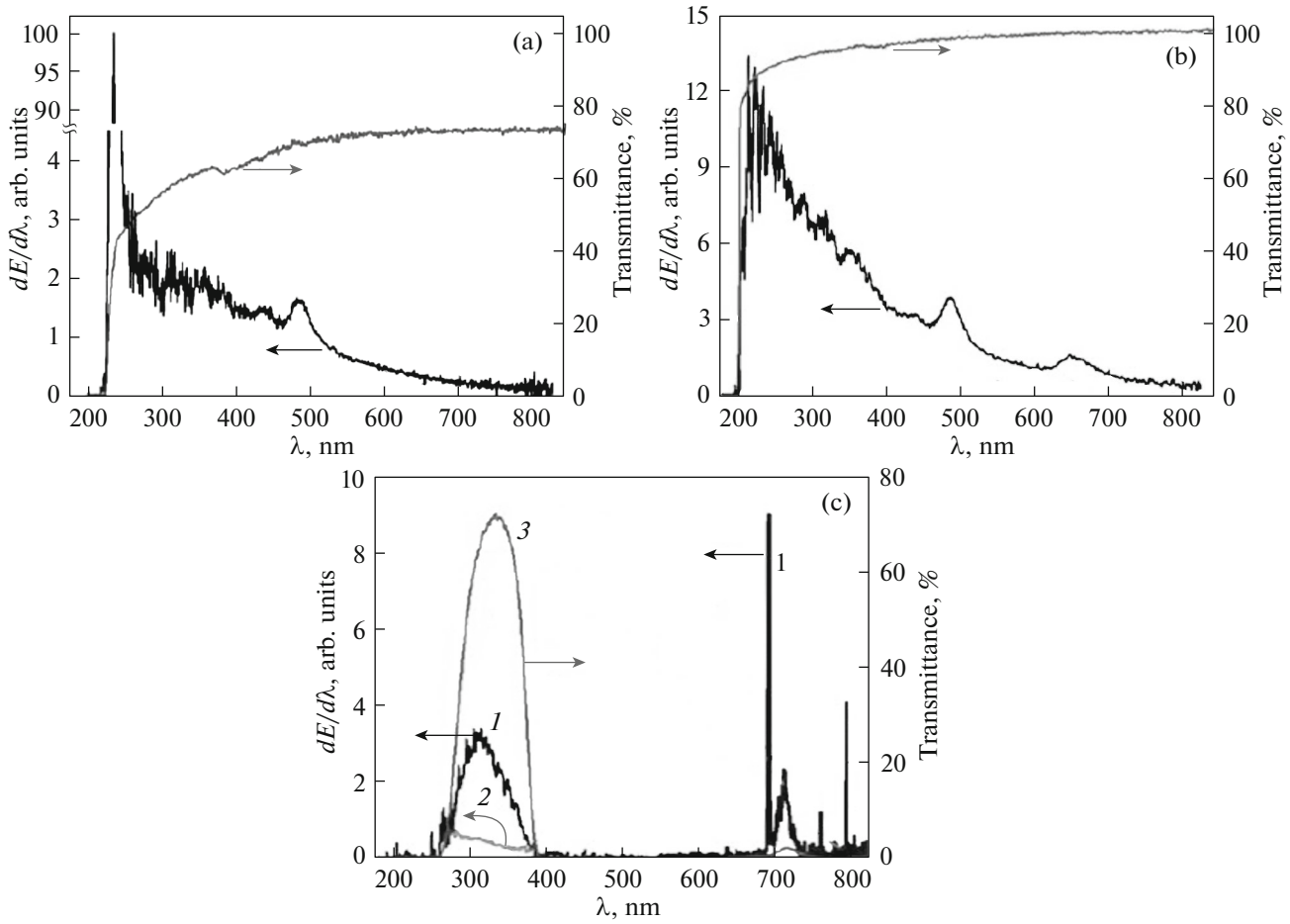

Fig. 16. Radiation and transmission spectrum of (a) C5 synthetic diamond, (b) KU-1 quartz glass, and (c) sapphire, where (*1*) emission spectrum obtained with the UFS-2 filter, (*2*) emission spectrum of sapphire in the range of 260–380 nm reconstructed with allowance for radiation absorption in the UFS-2 filter, and (*3*) transmission spectrum of this filter [42]. GIN-500 accelerator.

spectral energy density $dE/d\lambda$ increases monotonically with a decrease in the wavelength in the range of 220–450 nm. This is also related to VCR. At electron energies less than 200 keV, this band is absent because the threshold electron energy for VCR generation in quartz glass is 190 keV.

In sapphire, the same behavior of $dE/d\lambda$ was observed in the range of 250–450 nm. In addition, an intense narrow line with a maximum at a wavelength of 693 nm and a broad band in the 650–800 nm region were recorded; they are probably caused by uncontrolled impurity ions of Cr^{3+}. Figure 16c shows the emission spectrum of sapphire obtained using the UFS-2 filter, as well as the transmission spectrum of this filter and the emission spectrum of sapphire in the range of 260–380 nm. The spectrum was reconstructed taking into account the radiation absorption in the filter. As seen from the reconstructed spectrum, $dE/d\lambda$ increases with a decrease in the wavelength in the range of 260–380 nm. The transmission of sapphire corresponds to that of leucosapphire (Fig. 15c). The obtained results agree with the results of [34, 35, 40, 41, 92].

For additional identification of the nature of radiation in the UV range, the amplitude–time parameters of radiation were investigated using a PD025 photodiode and a UFS-1 filter. The combined use of the photodiode and filter allowed us to register the radiation mainly in the spectral range of 240–400 nm. As a result, the influence of the cathodoluminescence bands in the visible and infrared regions of the spectrum was minimized. The measurements show that the radiation pulse in all samples approaches the duration of the electron beam current pulse (Fig. 17).

The spectrum of diamond (Fig. 16a) shows that the radiative recombination band of free excitons prevails in the range of 230–245 nm. The spectral energy density of excitons emission is 10–50 times higher than the spectral energy density of VCR. According to the transmission spectrum of the UFS-1 filter (Fig. 14, curve *2*), its transmittance increases monotonically

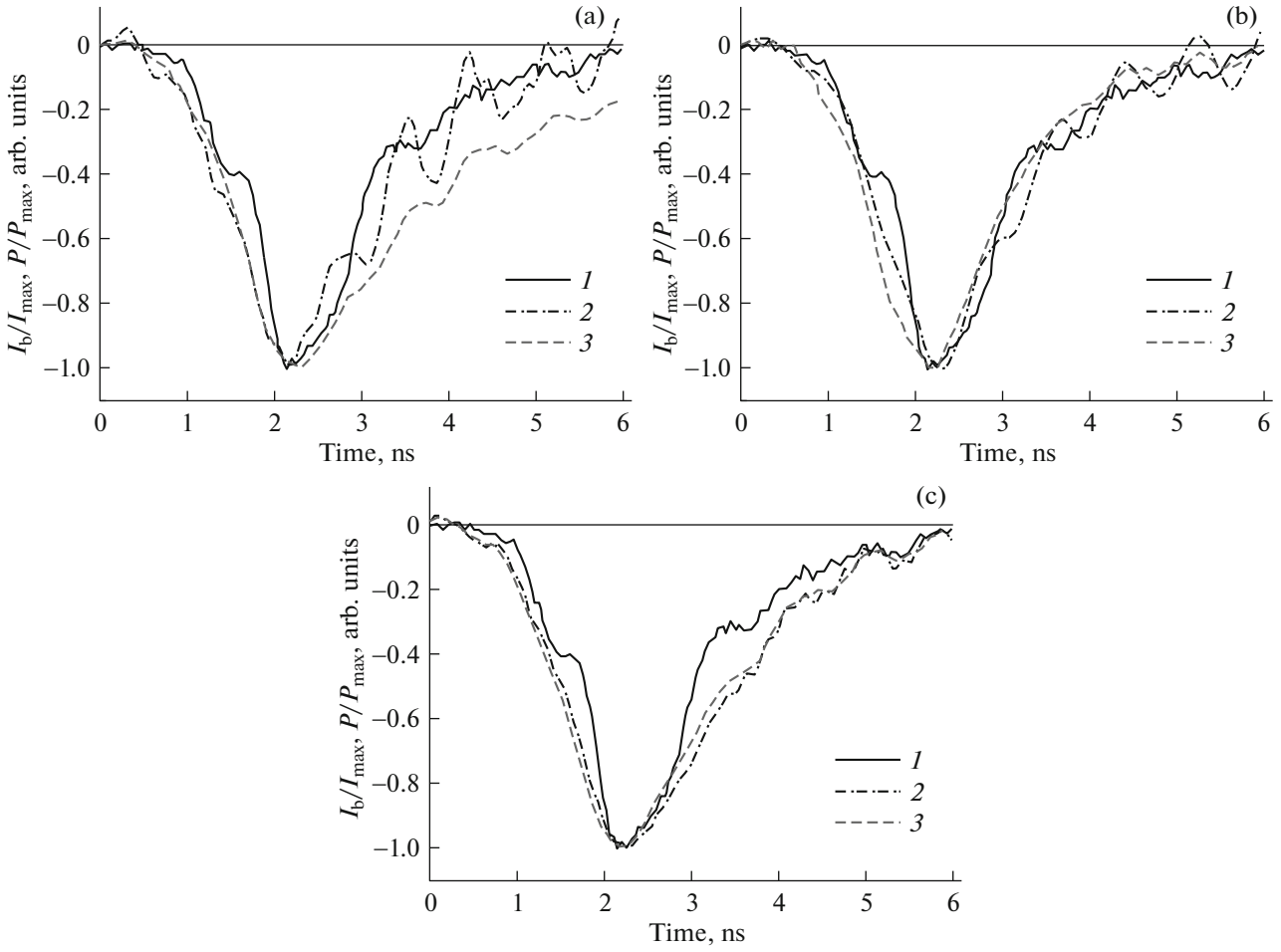

Fig. 17. (*1*) Time behavior of electron beam current pulses and emission of (a) diamond, (b) KU-1 quartz glass, and (c) sapphire detected (*2*) with the UFS-1 filter and (*3*) without it [42]. GIN-500 accelerator.

from 0 to 30% in the wavelength range from 230 to 245 nm. The UFS-1 filter transmits ~8% of exciton radiation which has a maximum at a wavelength $\lambda = 235$ nm. Therefore, as seen from Fig. 17a, the excitonic and other luminescence bands in the presence of the filter make an insignificant contribution to the luminescence of diamond because they are significantly attenuated by the filter. In the absence of a filter, the contribution of such bands to the emission in the diamond becomes significant, and the emission pulse detected without a filter is longer than the pulse obtained in the presence of a filter. Correpondingly, the contribution of the exciton band should be taken into account when creating Cherenkov detectors. Note that at temperatures above 200°C the luminescence in diamonds is quenched [90] and the exciton band is automatically suppressed. For quartz glass (Fig. 17b) and sapphire (Fig. 17c), the emission pulses are close in duration to electron beam current pulses, which indicates a significant fraction of VCR in their luminescence.

The luminescence of CaF_2, BaF_2–Ce, and MgF_2 fluorides was also studied on the facility with the GIN-500 accelerator [92]. The purpose of this work was to study PCL and VCR spectra in CaF_2, BaF_2, and MgF_2 crystals, to determine the region of the most intense bands, and to find out in which crystals the VCR intensity is the highest, as well as to determine the duration of radiation pulses upon excitation by an electron beam. Spectral studies of luminescence of samples under the action of an electron beam showed that the CaF_2 and BaF_2 crystals had the maximum radiation intensity in these conditions. The maximum of the exciton cathodoluminescence band of the CaF_2 crystal with a width of ~77 nm at half-maximum has a high intensity and falls at a wavelength $\lambda = 280$ nm. The decay kinetics of this band is described by an exponential function with a relaxation time of ~70 ns, which exceeds the RE beam current pulse duration by an order of magnitude. Correspondingly, it is very difficult to distinguish the VCR contribution to the emission of the CaF_2 crystal. Also, the oscillograms

showed an increase in the PCL intensity during the second pulse of the electron beam current with an energy that is less than the threshold energy for VCR (E_{th} = 202 keV).

The emission spectrum of the BaF_2–Ce crystal consisted of a band corresponding to electron transitions from the valence band formed by 2*p*-states of F to the upper core zone of the crystal formed by the 5*p*-state of Ba^{2+} (cross-luminescence): a narrow band with a maximum at $\lambda = 217$ nm and a half-width of 30 nm. The broad excitonic band with a maximum at $\lambda = 308$ nm has a half-width of 90 nm. The band intensities are ~600 and ~1150 arb. units, respectively. The third band with a maximum at $\lambda = 483$ nm corresponds to transitions from the fluorine ions of the second coordination sphere the low intensity of which (~35 arb. units) is associated with a small degree of overlapping between the cation and anion wave functions. The strong drop in transmission in the spectral region shorter than 400 nm is caused by the absorption by Ce^{3+} ions at *f*–*d*-transition. It is known that BaF_2 is the fastest of known inorganic scintillators, which is corroborated by good coincidence of time behavior of its emission with the shape of electron beam current pulses, as it was obtained with GIN-500. However, the increase in the radiation intensity during the second pulse of the electron beam with the energy less than the threshold energy for VCR excludes the presence of VCR during the second pulse. Thus, the detected emission of CaF_2 and BaF_2 crystals is mainly related to PCL.

In the MgF_2 crystal at low temperatures during pulsed irradiation with an electron beam, autolocalized excitons with corresponding radiative transitions at a wavelength of $\lambda = 387$ nm are predominantly created [93]. With an increase in temperature, the luminescence intensity of this band decreases; at temperatures above 100 K, the spectrum is dominated by an edge band with a maximum at $\lambda = 295$ nm. In the experiments with GIN-500, cathodoluminescence of the MgF_2 crystal had a low intensity, which facilitated VCR detection on the PCL background. A broad band of emission in the wavelength range shorter than 400 nm the intensity of which increased with a decrease in the wavelength was related to VCR. The time behavior of the MgF_2 crystal emission and the first pulse of electron beam current coincided well, which is also typical for VCR. In addition, during the second pulse of the electron beam current with an energy less than the threshold energy for VCR (~200 keV), radiation was absent. Thus, exposure of MgF_2 crystals which have a low PCL intensity in the shortwave region of the spectrum to a beam of electrons with energies of up to 350 keV made it possible to detect VCR.

One of the most accessible and relatively inexpensive materials with good transparency in the optical range of the spectrum and a sufficiently high refractive index (~2) is yttrium oxide ceramics used in optical devices and lasers. In [76], the luminescence of yttrium oxide ceramics was studied on the facility with the GIN-500 accelerator. In the course of the experiments, the emission spectrum of the ceramic sample during its irradiation with an electron beam was taken, as well as the transmission spectrum of the sample. With a decrease in the wavelength, the intensity of the spectrum increases up to the transmittance limit of the material. Such spectrum behavior is typical for VCR [34, 35, 94]. It is also corroborated by good coincidence of the experimental emission spectrum of the sample with the calculated VCR spectrum calculated [95] taking into account the real energy distribution of beam electrons, dispersion of refractive index of the ceramics, and its transmission spectrum. In the wavelength range of 450–550 nm, a band which can be associated with cathodoluminescence of ceramics was observed. The time characteristics of the glow of the ceramic sample correspond to the beam current pulse. Since the Vavilov–Cherenkov effect is almost free from time lag, the VCR duration should coincide with the beam current duration, which was observed in the experiment [76]. Analysis of the obtained data unambiguously testifies that VCR was recorded in the experiments, and its energy in yttrium oxide ceramics exceeds the energy of cathodoluminescence.

4.2. Spatial Characteristics of VCR and PCL

For relatively low electron energies ($E_e \le 50$ keV, $\beta < 0.44$), the process of multiple scattering results in the fact that VCR photons are emitted over a wide range of angles even in thin radiators. As the electron energy increases, the multiple scattering decreases and the angular VCR distribution becomes more directional. For example, for electron energy $E_e = 1$ MeV, the angle of multiple scattering $\langle\theta_{ms}\rangle$ 50-μm-thick quartz glass plate does not exceed 25°, whereas the VCR angle $\theta = 47°$. With a further increase in the electron energy, a suitable geometry must be chosen to extract VCR out of the plate. Only when the plate is tilted by an angle ψ with respect to the velocity vector of the electron beam a part of the VCR cone will escape into the air at an angle φ (Fig. 18a):

$$\varphi = \psi + \arcsin\left[n\cos(\theta + \psi)\right]. \quad (8)$$

For a nondivergent electron beam, VCR can be extracted from a quartz glass target into vacuum (or air) only for angles of inclination $\psi < 86°$. For example, for an inclination angle $\psi = 70°$, the maximum VCR output corresponds to an output angle $\varphi = 29°$ (8). If we choose the inclination angle $\psi = 43°$, which corresponds to the angle $\theta = 47°$, VCR will exit the quartz glass plate without refraction, i.e., at the angle

$$\varphi = \frac{\pi}{2} - \theta = 43°.$$

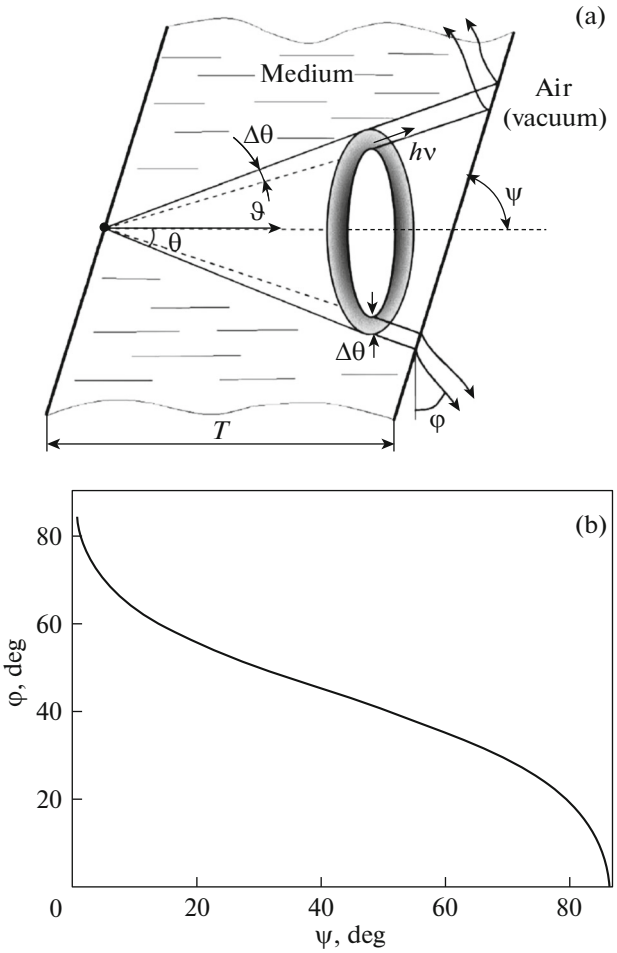

Fig. 18. (a) Angular VCR distribution when passing from the medium to air (vacuum) and (b) dependence of the angle φ on the plate inclination angle ψ [41].

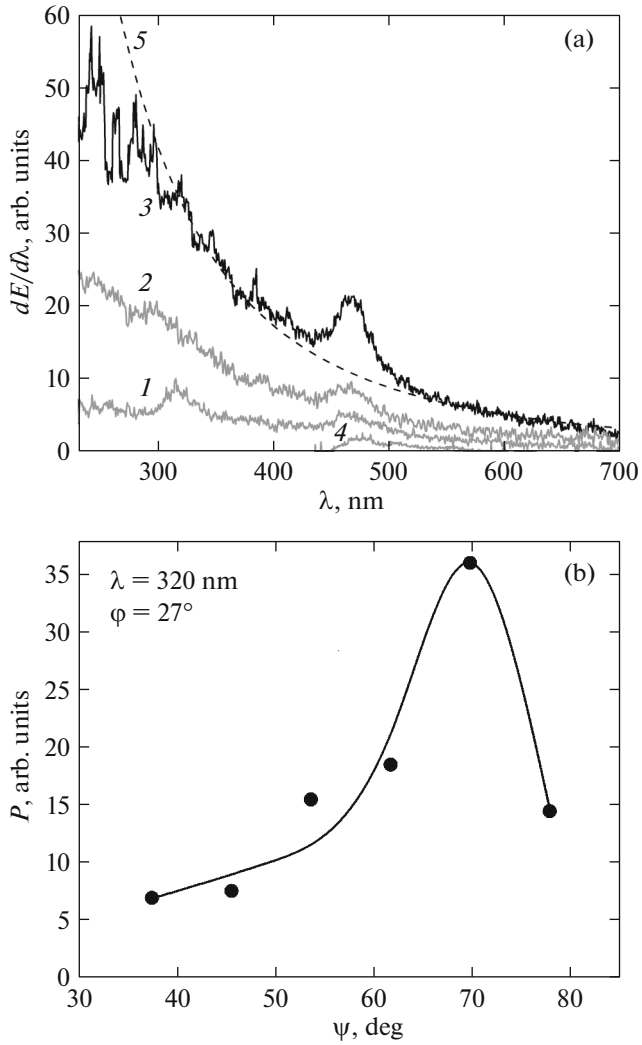

Fig. 19. (a) Radiation spectra of a GE-014 quartz glass plate at different angles ψ between the surface of the plane-parallel plate of quartz glass and direction of the electron flux: (*1*) 46°, (*2*) 54°, (*3*) 70°, and (*4*) 86° and (*5*) calculated VCR spectrum for the electron energy of 6 MeV [41]. Spectra *3* and *5* are normalized to intensity at the wavelength of 350 nm. (b) Dependence of the radiation intensity at the wavelength λ = 320 nm on the angle ψ between the plane of the quartz glass plate and direction of the electron flux.

In a medium, the angular VCR distribution has azimuthal symmetry (Fig. 18a) and can be estimated as $\Delta\theta_1 \approx \sqrt{\theta_{ms}^2 + \theta_e^2}$, where θ_{ms} is the root-mean-square angle of multiple scattering at a length $T/2$ and θ_e is the initial divergence of the beam. In the approximation $\Delta\theta_1 \to 0$, relationship (8) yields an unambiguous relation between the angle of VCR output into the air and target inclination ψ (Fig. 18a); for any ψ, only a part of the VCR cone is extracted. Broadening of the Cherenkov cone $\Delta\theta_1$ breaks the rigid connection between the angles ψ and φ; however, if the angle φ means the angle corresponding to the maximum of the VCR output, the plot in Fig. 18b illustrates this connection.

The Vavilov–Cherenkov radiation in quartz glass has the smallest angle θ, which facilitates its extraction from a plane-parallel plate. For this reason, the main attention in [41] was paid to the study of VCR in quartz glass. The available diamond samples were too small, and the sapphire and leucosapphire samples at electron beam energy of 6 MeV darkened under the action of the electron beam and X-ray radiation.

The emission spectra of the GE-014 quartz glass plate at different angles between the surface of the plane-parallel plate and the direction of the electron flux are presented in Fig. 19. The position of the light guide delivering the radiation from the quartz glass plate to the spectrometer did not change with a change in the angle ψ. This angle between the lightguide axis and the normal to the direction of the electron beam in the beam was φ = 27°. It is seen from the figure that the radiation energy distribution in the spectrum

changes depending on the angle between the plane of the plane-parallel plate of quartz glass and the direction of the electron flux in the beam. At an angle $\psi \approx 70°$ in the UV region, the highest spectral energy density of radiation registered by the spectrometer is observed. This spectrum is similar to the VCR spectrum calculated by formula (5) with allowance for the dispersion of the refractive index (curve *5* in Fig. 19a). The correspondence of VCR to the radiation detected in the UV region corroborates the dependence of its spectrum on the angle between the plate and the electron flux. The angle of rotation of the quartz glass plate $\psi \approx 70°$ relative to the electron beam direction provided the greatest efficiency of VCR extraction, which well agrees well with the estimate by formula (8) from which it follows that $\varphi = 29°$. When the angle of plate rotation increased or decreased, the VCR intensity decreased. The radiation in the wavelength region of 450–600 nm can be referred to PCL.

Figure 19a presents the calculated VCR spectrum normalized by the intensity at a wavelength $\lambda = 350$ nm to the experimental spectrum obtained at the angle $\psi = 70°$ between the quartz glass plate and the electron beam. The radiation intensity on both spectra in the region shorter than 450 nm increases with a decrease in the wavelength. This fact, as well as the dependence of the radiation intensity on the angle between the plane of the quartz glass plate and the direction of the electron beam (Fig. 19b), unequivocally proves the detection of VCR spectra in this work. It should be noted that a change in the inclination angle by 25° (from $\psi = 70°$ to $\psi = 45°$) leads to a fivefold decrease in the intensity but not to zero, which is explained by broadening of the VCR cone $\Delta\theta_1 = 26°$.

Thus, in [41], the VCR spectrum in the UV and visible regions was recorded for the first time upon excitation of GE-014 and KU-1 quartz glass plates by an electron beam with an energy of 6 MeV. It was shown that changing the angle between the surface of the plane-parallel plates and the direction of the electron beam significantly affected both the VCR intensity and the emission spectrum. At large and small angles of plate inclination, PCL is registered in the visible region of the spectrum, and the VCR intensity becomes low.

5. PCL AND VCR IN POLYMETHYLMETHACRYLATE

5.1. General Information and Amplitude–Time Characteristics

Polymethylmethacrylate is widely used as a material for the radiator in detectors of pulsed bremsstrahlung radiation and electron beam. This is due to the ease of fabrication of PMMA radiators, as well as the low level of luminescence, 2–7% of VCR (data obtained for γ-quanta with an energy of 1 MeV) [96]. Polymethylmethacrylate is also used in scintillation detectors as a base in which the fluorescent agent is dissolved [46]. The transparency range of PMMA depends on the presence of impurities and is approximately 350–2000 nm. The refractive index of PMMA is $n_D = 1.49$ and the threshold energy for the VCR appearance for electrons $E_{th} = 178$ keV. In addition, PMMA is one of the common materials in the manufacture of plastic light guides. Such light guides are used in scintillation detectors used in radiation therapy to determine the absorbed dose [46, 97]. Polymethylmethacrylate and polystyrene from which plastic optical fibers are commonly made have characteristics equivalent to those of biological tissues or water as dosimetric materials [98]. However, since the light guide, as well as the scintillator, is exposed to a beam of ionizing radiation, VCR and PCL are excited in it, which distorts the useful signal coming to the radiation receiver. In the English-language literature, these distortions of the useful VCR signal are called the stem effect [47]. However, at electron energies of ~1 MeV and higher, the relatively low PCL level makes PMMA a promising material for the manufacture of plastic optical fibers. Therefore, VCR arising in plastic optical fibers finds useful applications in plastic fiber optic dosimeters [44].

In a series of works devoted to medical dosimetry [44, 45, 47], PMMA luminescence under the action of ionizing radiation (primarily, electrons and high-energy photons) was investigated, including detection of the spectrum of radiation which passed through a light guide. It should be noted that when PMMA samples are irradiated with high-energy photons, recoil electrons with energies of tens or hundreds of kiloelectronvolts are generated in PMMA due to Compton scattering, which to a certain extent corresponds to the situation of sample interaction with electron beams of this energy range. Taking into account the high demand for PMMA as a material for the radiator in Cherenkov detectors, as a light guide transmitting radiation in scintillation dosimeters, as well as the use of PMMA as a plastic base in organic scintillators, there is the necessity of a more detailed study of PMMA characteristics upon irradiation with ionizing radiation, including electron fluxes with energy of hundreds of kiloelectronvolts.

Studies of the PMMA emission characteristics upon RE excitation were initiated in [48, 49]. It was reported about detection of amplitude–time characteristics of VCR arising under the action of a subnanosecond RE beam generated in air at atmospheric pressure. However, the temporal resolution of the instrumentation used was small, and no spectral studies of PMMA luminescence were performed.

As shown above with samples of other materials, to determine the VCR and PCL contributions to the signal detected by the photodetector, it is necessary to know the emission spectra. Such a cycle of investigations has been carried out in [50–52, 94]. The

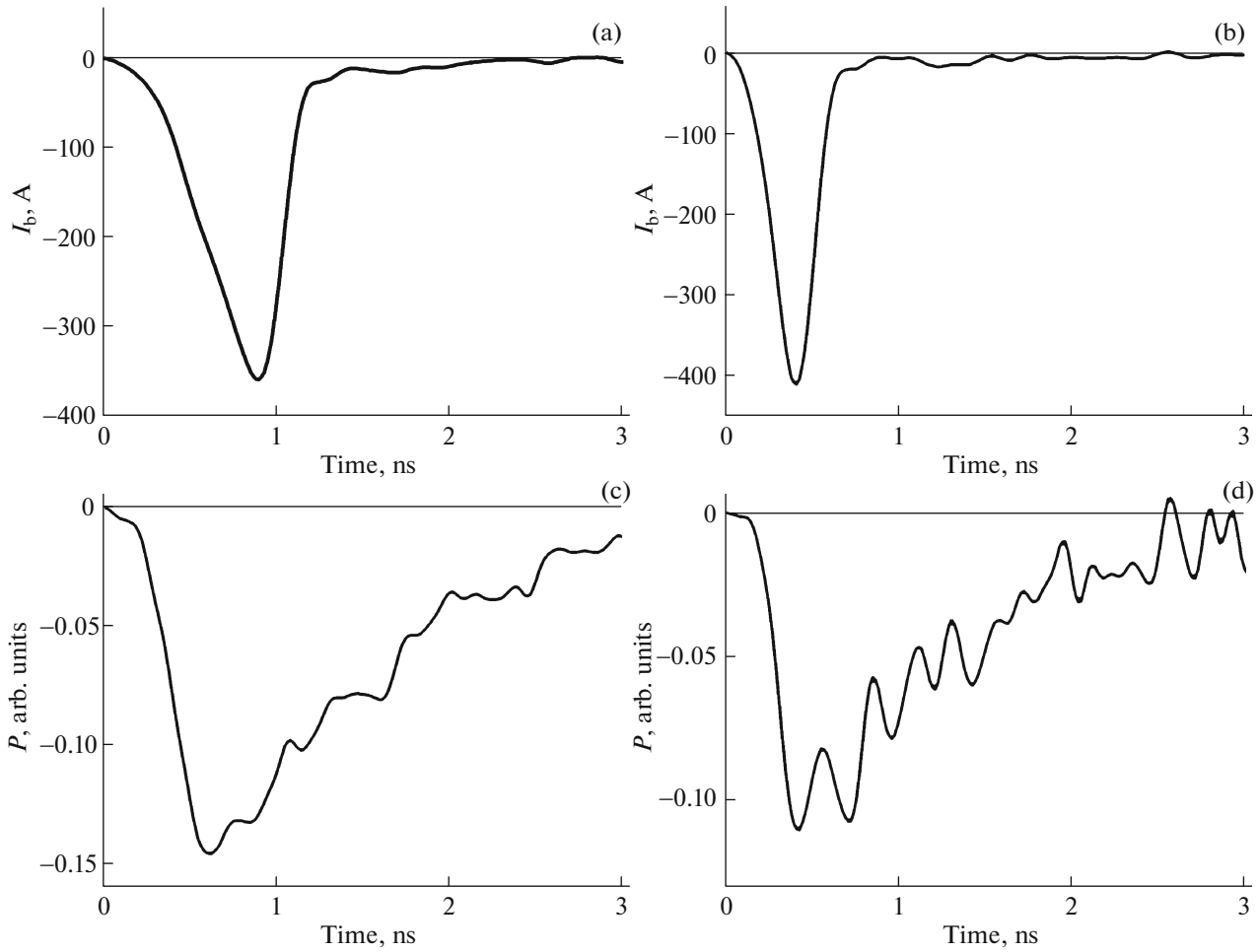

Fig. 20. (a, b) Pulses of the RE beam current and (c, d) oscillograms of radiation pulses of the 6-mm-thick PMMA sample under helium pressure of (a, c) 15 and (b, d) 30 Torr in the gas-filled diode [51]. The interelectrode gap in the gas-filled diode d = 14 mm. The transmission band of the oscilloscope is 6 GHz.

SLEP-150M electron accelerator was used to obtain amplitude–time characteristics of PMMA luminescence. The electron beam spectrum is presented in Fig. 6a. The schematic of the experiments is shown in Fig. 9b.

Figure 20 presents pulses of the RE beam current and PMMA glow. The largest amplitudes of PMMA glow pulses are observed at the highest number of electrons in the beam current. The duration of the glow pulse at half-maximum was several times longer than the duration of the RE beam current pulse. Note that PMMA samples used in these experiments were from different batches and had different thicknesses; however, the PMMA emission pulses had approximately the same shape and duration at half-maximum. Based on the obtained amplitude–time characteristics of the PMMA emission, it can be stated that VCR in the experiments described in [48, 49] also did not make a significant contribution to the detected PMMA luminescence.

5.2. Spectral Characteristics of the PMMA Luminescence

The spectral characteristics of PMMA luminescence under the action of an electron beam were also studied using the SLEP-150M accelerator with a sleeve cathode. In addition, a KrCl-excilamp was used to excite photoluminescence. Schematics of the experiments are shown in Fig. 9a. The investigations of the PMMA luminescence and transmission spectra with different samples showed that the emission and transmission spectra in three samples were not significantly different. The PMMA luminescence spectra, together with transmission spectra, are presented in Fig. 21. The strong absorption of both samples begins in the region of the spectrum shorter than 350 nm. In the region with low absorption of PMMA one can see only one band with the maximum spectral energy density at a wavelength of ~490 nm. The Vavilov–Cherenkov radiation was not detected, which is associated with its

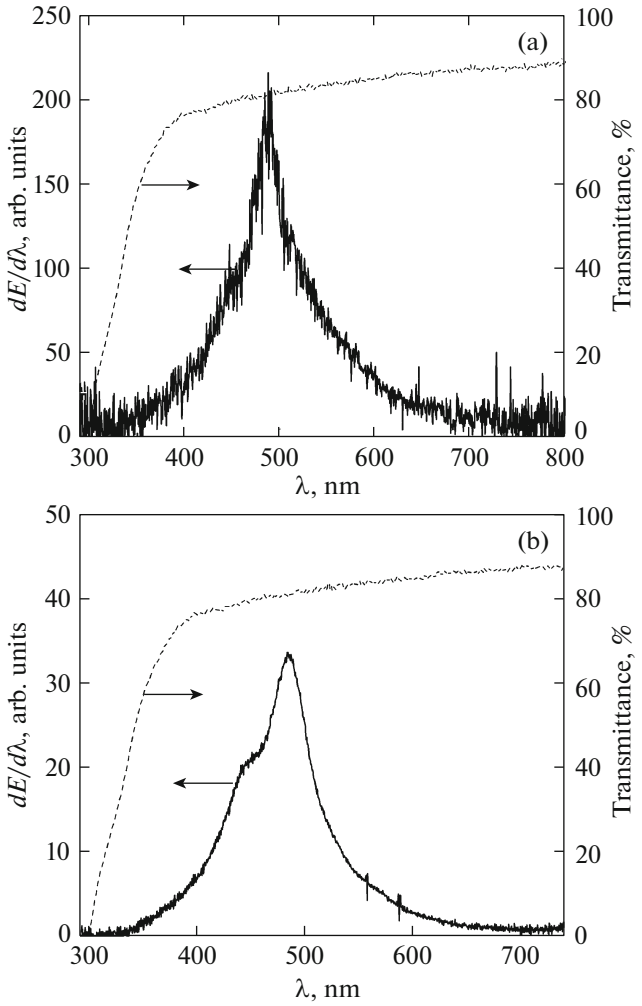

Fig. 21. Spectra of emission (solid curves) and transmission (dashed curves) of a 6-mm-thick PMMA sample upon excitation by (a) an electron beam and (b) an excilamp [51].

low intensity when using the SLEP-150M accelerator as compared to the intensity of luminescence.

The intensity of PMMA luminescence increased with an increase in the number of electrons in the SAEB. However, the shape of the emission spectra in the three PMMA samples coincided and did not depend on the amplitude and duration of the beam current pulse. The luminescence spectra showed a band with a maximum in the region of 490 nm. Its position did not change when the SAEB current density was changed. The shortwave absorption boundary of PMMA, which lies for three samples in the region of 300 nm, has no effect on the shape of the emission spectrum.

In one of the PMMA samples (3-mm-thick), a second band with a maximum in the region of 400 nm was detected in the luminescence spectrum. A sharp decrease in the emission intensity of this band in the UV region of the spectrum coincides with an increase in the absorption of this sample in the region of 350–400 nm. The shift of the shortwave boundary of the transmission band in the 3-mm-thick PMMA sample to the longwave region (as compared to other samples) can be explained by the presence of additional impurities in the sample. However, the band with a maximum in the region of 400 nm cannot be attributed to VCR because a similar band is absent in other PMMA samples with the same refractive index in which absorption in the region of 350–400 nm is low.

This conclusion is also corroborated by the emission spectrum of this plate when excited with a KrCl-excilamp with a wavelength of 222 nm. As under SAEB excitation, there are two emission bands in this sample. The shape of these bands upon excitation by an electron beam and UV excilamp radiation is approximately the same, and the excilamp radiation hardly leads to the appearance of VCR. It can be seen from Fig. 21 that the emission spectra of a 6-mm-thick PMMA sample under excitation by an excilamp and an electron beam are also almost identical. A similar spectrum was also registered for samples with thicknesses of 0.9 and 10 mm. This additionally corroborates that the nature of the observed emission in these experiments is related to PCL.

The performed investigations allowed us to establish a very important feature which follows from the experiments with the excilamp. The ultraviolet radiation of the excilamp leads to the appearance of a luminescence band with the maximum intensity at a wavelength of ~490 nm. In the 3-mm-thick sample, in addition, a second band in the region of 350–450 nm is detected. Correspondingly, one should expect that VCR in the UV region of the spectrum will lead to the enhancement of luminescence intensity in PMMA in the visible region of the spectrum. It is known that the VCR intensity increases with a decrease in the wavelength and an increase in the electron energy. Thus, VCR with a wavelength shorter than 300 nm which is generated and then absorbed in PMMA should enhance the luminescence intensity at a wavelength of ~490 nm. At the same time, the ratio of VCR and luminescence intensities should depend on the energy distribution of beam electrons.

5.3. PMMA Destruction under the Action of an Electron Beam

Experiments on studying PMMA destruction and the nature of sample luminescence under electron beam irradiation [52] were carried out on two facilities: with the SLEP-150M accelerator to which a gas-filled diode was connected and with the GIN-600 accelerator to which a vacuum diode was connected. The parameters of the GIN-600, as well as those of the SLEP-150M, are presented in Section 2. The electron beam energy densities (H) in the experiments varied

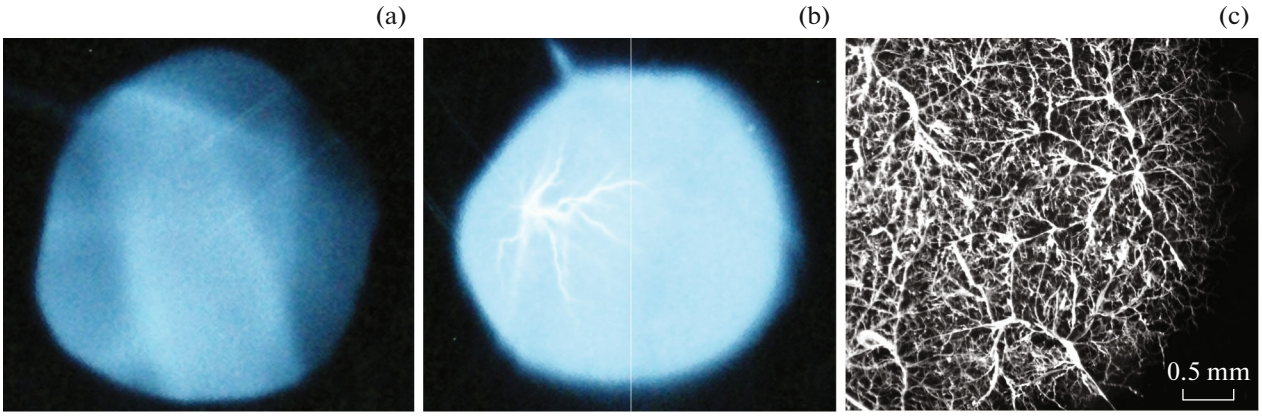

Fig. 22. Photographs of PMMA luminescence in one pulse after (a) some first excitation pulses and (b) 100 or more excitation pulses. (c) Morphology of residual destructions formed in the deceleration zone of SAEBs as a result of the development of the electric breakdown [51]. The diameter of the (a, b) luminous region and (c) the destruction zone the image of which is magnified is ~6 mm. The number of irradiation pulses is ~500 at a frequency of 1 Hz. SLEP-150M accelerator.

from 10^{-4} to 0.4 J/cm^2, and the beam current pulse durations at half-maximum were 0.1–0.6 ns and 12 ns.

When the PMMA plates (with thicknesses of 0.9, 3, 6, and 10 mm) were excited with an electron beam, a blue glow was observed. Its intensity increased with an increase in the amplitude and duration of the SAEB pulse. The glow of all plexiglas plates at atmospheric pressure of helium, nitrogen, and air in the gas-filled diode and beam electron density per square centimeter ~2×10^{10} was weak, so it could be detected only visually when the room with the setup was completely darkened.

Figure 22 presents photographs of PMMA luminescence at maximum electron beam energy densities (~0.01 J/cm^2) after (a) some first excitation pulses and (b) 100 or more excitation pulses. Analysis of the photographs shown in Fig. 22 indicates that in the first excitation pulses and at maximum beam current densities ($H \sim 0.01$ J/cm^2), as well as at low SAEB current densities ($H \leq 0.001$ J/cm^2), a relatively uniform cathodoluminescence of samples over the irradiated surface is observed. The observed inhomogeneities in Fig. 22a are related to fluctuations in the beam current density in individual pulses. An increase in the number of irradiation pulses at $H \approx 0.01$ J/cm^2 resulted in accumulation of the negative SAEB bulk charge injected into the sample and initiation of the electric breakdown of PMMA in the deceleration zone of the electron beam with the highest density. The electric breakdown is implemented in the form of streamer discharges (SDs). Electric discharges are detected both by the glow of the dense plasma formed in electric breakdown channels (EBCs) (Fig. 22b) and by the morphology of residual destructions fractures (Fig. 22c). The duration of the glow of the plasma formed in the EBCs at $H < 0.01$ J/cm^2 could not be detected with the PD025 photodiode due to the low intensity of the SD radiation as compared to the PCL intensity. The predominance of the solid SD emission spectrum over PCL occurred upon excitation by the GIN-600 accelerator at a beam energy density $H >$ 0.2 J/cm^2 [52], which corresponds to the threshold of the SD formation and appearance of residual EBCs in this material.

Thus, results of experimental investigations of PMMA emission upon excitation by an RE beam and a KrCl-excilamp with an emission wavelength of 222 nm show that the PCL band with a maximum at a wavelength of ~490 nm makes the main contribution to the emission in both cases. The luminescence intensity of this band varies in proportion to the number of electrons in the beam, which allows this radiation to be used for the determination of the number of high-energy electrons in electron beams. Based on experiments with the excilamp, it is assumed that VCR with wavelengths shorter than 300 nm should enhance the luminescence intensity at the ~490 nm band. In the presence of impurities in PMMA samples, a second luminescence band with a maximum at a wavelength of ~400 nm can be detected.

Multipulse irradiation of PMMA by SAEBs at $H \geq 0.01$ J/cm^2 results in an electric breakdown inside the sample due to the accumulation of a negative electron beam bulk charge and the formation of a strong electric field in the beam deceleration zone. Electrical discharges are detected both by the glow of the dense plasma formed in the EBC and by the morphology of the residual destructions. At electron energy of up to 400 keV, VCR was not detected on the GIN-600 facility in PMMA [52]. Apparently, the intensity of the continuous spectrum of SD radiation significantly exceeded not only PCL but also VCR.

The complexity of VCR detection in PMMA at beam electron energies of hundreds of kiloelectron-

volts is caused by the following. First, PMMA has a low damage threshold due to the breakdown by beam electrons accumulated in the dielectric. Second, strong absorption in PMMA begins as early as from 300–350 nm, and the VCR intensity increases in inverse proportion to the cube of the wavelength. Third, PMMA has a relatively low refractive index $n_D = 1.49$; correspondingly, the threshold electron energy is $E_{th} = 178$ keV. All electrons with energy below the threshold excite cathodoluminescence on the background of which VCR is hard to distinguish. However, reduction of the beam current pulse duration to 350 ps and an increase in the electron energy to 450 keV made it possible to detect VCR in PMMA on the background of PCL with a high energy density [99].

6. CONCLUSIONS

The presented investigations of luminescence excited in different samples by electron beams with the subnanosecond and nanosecond duration made it possible to detect VCR spectra in the UV and visible ranges in diamond (natural and synthetic), quartz glass, sapphire, leucosapphire, MgF_2, Ga_2O_3, and other transparent materials. Conditions at which VCR can be detected at a beam electron energy of up to 350 keV using a standard spectrometer have been determined. Calculations taking into account the influence of electron energy and refractive index of the substance on the VCR intensity and spectrum, as well as on spatial characteristics of the radiation, corroborate the obtained experimental data on the influence of electron energy on VCR spectra. It has been found that VCR detection is impeded in PMMA due to radiation absorption in the range shorter than 300–350 nm, as well as due to the internal breakdown of samples as a result of electron accumulation in them at high beam current densities or/and long pulse durations. To detect VCR on the background of PCL in PMMA samples, it is necessary to increase the electron energy, which was demonstrated in [99] at a subnanosecond duration of the beam current pulse.

As follows from the performed analysis of the obtained data about emission spectra of different samples, parameters of electron beams (in particular, runaway electron beams) can be detected using both PCL and VCR. This is corroborated by a recent work [100]. When studying the RE generation in the IR-T1 Tokamak facility, two LYSO scintillation crystals ($Lu_{1.8}Y_{0.2}SiO_5$:Ce) were used for the detection. They were placed in a graphite case and separated by a graphite filter. Using PCL is more expedient at electron energies of up to 200–300 keV because the PCL intensity in most of transparent materials significantly exceeds the VCR intensity. In addition, PCL is emitted in all directions relative to the direction of beam electrons, which facilitates its detection. Among the samples under study, one can recommend for the creation of electron detectors ZnS and ZnSe crystals which have a high PCL intensity and high radiation resistance. Besides, in these crystals, the amplified spontaneous emission mode is possible [89], which must increase the efficiency of the radiation outcoupling from the irradiation zone.

Detection of electron beam parameters using VCR has advantages at electron energies of ~400 keV and higher. Among the studied samples, the most promising one for the creation of VCR detectors is type IIa synthetic diamond obtained by gas-phase deposition, as well as (at sufficiently high electron energies) quartz glass with high transmission in the UV spectral range (e.g., KU-1). When designing VCR detectors, one should take into account the angular distribution of the radiation and internal reflection. For diamond, in addition, one should take into account the appearance of an intense exciton band with an increase in the beam current density in a diamond with a maximum at a wavelength of 235 nm.

At high electron energies, one should take into account the radiation damage of samples. For example, as shown by experiments at electron energy of 6 MeV, sapphire and leucosapphire samples rapidly became dark under the action of a powerful and high-energy X-ray radiation. It is well known that the generation efficiency of X-ray radiation significantly increases with an increase in the electron energy of >1 MeV [101]. The feature of PMMA samples is their rapid destruction by discharges appearing in the dielectric at high densities and long durations of the electron beam current.

In [102], it was reported about VCR detection near the Earth's surface under the action of the solar wind. We hope that this survey will heighten the interest in studying spectral and amplitude–time VCR characteristics (in particular, in different gases and liquids).

ACKNOWLEDGMENTS

We are grateful to our colleagues S.B. Alekseev, D.V. Beloplotov, A.V. Vukolov, E.I. Lipatov, M.I. Lomaev, V.I. Oleshko, A.P. Potylitsyn, I.A. Prudaev, D.A. Sorokin, and others with whom the joint investigations of VCR and PCL characteristics were carried out.

FUNDING

The work on studying VCR and PCL characteristics in 2018–2020, as well as writing this survey, were supported by the Russian Science Foundation, project no. 18-19-00184.

CONFLICT OF INTEREST

The authors declare that they have no conflicts of interest.

REFERENCES

1. P. Cherenkov, in *Nobel Lectures, Physics: 1942–1962* (Nobel Foundation Staff, Elsevier, 1964). https://doi.org/10.1016/C2013-0-07831-0
2. T. Sumiyoshi, I. Adachi, R. Enomoto, T. Iijima, R. Suda, M. Yokoyama, and H. Yokogawa, J. Non-Cryst. Solids **225**, 369 (1998). https://doi.org/10.1016/S0022-3093(98)00057-X
3. V. P. Zrelov, *Vavilov-Cherenkov Radiation and its Application in High-Energy Physics, Part 2* (Atomizdat, Moscow, 1968) [in Russian].
4. B. M. Bolotovskii, Phys. Usp. **52**, 1099 (2009). https://doi.org/10.3367/UFNr.0179.200911c.1161
5. V. Ginis, J. Danckaert, I. Veretennicoff, and P. Tassin, Phys. Rev. Lett. **113**, 167402 (2014). https://doi.org/10.1103/PhysRevLett.113.167402
6. X. Lin, S. Easo, Y. Shen, H. Chen, B. Zhang, J. D. Joannopoulos, M. Soljačic, and I. Kaminer, Nat. Phys. **14**, 816 (2018). https://doi.org/10.1038/s41567-018-0138-4
7. A. P. Potylitsyn and S. Y. Gogolev, Phys. Part. Nucl. Lett. **16**, 127 (2019). https://doi.org/10.1134/S1547477119020110
8. G. S. Bowers, W. Blaine, X. M. Shao, B. Dingus, D. M. Smith, M. Schneider, F. Martinez-McKinney, M. P. McCarthy, S. BenZvi, L. Nellen, and N. Fraija, Phys. Rev. D **100**, 043021 (2019). https://doi.org/10.1103/PhysRevD.100.043021
9. S. I. Akasofu and S. Chapman, *Solar-Terrestrial Physics* (Clarendon, Oxford, 1972). https://doi.org/10.1002/qj.49709942230
10. S. L. Valley, *Handbook of Geophysics and Space Environments* (McGraw-Hill, New York, 1965).
11. Y. Tsunesada, R. Katsuya, Y. Mitsumori, K. Nakayama, F. Kakimoto, H. Tokuno, N. Tajima, P. Miranda, J. Salinas, and W. Tavera, Nucl. Instrum. Methods Phys. Res., Sect. A **763**, 320 (2014). https://doi.org/10.1016/j.nima.2014.06.054
12. K. D. Vries, A. M. Berg, O. Scholten, and K. Werner, Phys. Rev. Lett. **107**, 061101 (2011). https://doi.org/10.1103/PhysRevLett.107.061101
13. L. D. Landau, J. S. Bell, M. J. Kearsley, L. P. Pitaevskii, E. M. Lifshitz, and J. B. Sykes, *Electrodynamics of Continuous Media* (Pergamon, Oxford, 1984).
14. A. V. Vukolov, A. I. Novokshonov, A. P. Potylitsyn, and S. R. Uglov, J. Phys.: Conf. Ser. **732**, 012011 (2016). https://doi.org/10.1088/1742-6596/732/1/012011
15. K. I. Nanbu, Y. Saito, and H. Saito, Particles **1**, 305 (2018). https://doi.org/10.3390/particles1010025
16. V. V. Plyusnin, L. Jakubowski, J. Zebrowski, H. Fernandes, C. Silva, K. Malinowski, P. Duarte, M. Rabinski, and M. J. Sadowski, Rev. Sci. Instrum. **79**, 10F505 (2008). https://doi.org/10.1063/1.2956960
17. L. Jakubowski, M. J. Sadowski, J. Zebrowski, M. Rabinski, K. Malinowski, R. Mirowski, Ph. Lotte, J. Gunn, J.-Y. Pascal, G. Colledani, V. Basiuk, M. Goniche, and M. Lipa, Rev. Sci. Instrum. **81**, 013504 (2010). https://doi.org/10.1063/1.3280221
18. L. Jakubowski, M. J. Sadowski, J. Zebrowski, M. Rabinski, M. J. Jakubowski, K. Malinowski, R. Mirowski, Ph. Lotte, M. Goniche, J. Gunn, G. Colledani, J.-Y. Pascal, and V. Basiuk, Rev. Sci. Instrum. **84**, 016107 (2013). https://doi.org/10.1063/1.4776190
19. F. Bagnato, A. Romano, P. Buratti, A. Doria, L. Gabellieri, E. Giovenale, A. Grosso, L. Jakubowski, D. Pacella, and V. Piergotti, Plasma Phys. Control. Fusion **60**, 115010 (2018). https://doi.org/10.1088/1361-6587/aae0b3
20. M. R. Ghanbari, M. Ghoranneviss, A. S. Elahi, S. Mohammadi, and R. Arvin, J. Fusion Energy **35**, 180 (2016). https://doi.org/10.1007/s10894-015-9992-6
21. B. Pourshahab, M. R. Abdi, A. Sadighzadeh, and C. Rasouli, Phys. Plasmas **23**, 072501 (2016). https://doi.org/10.1063/1.4955218
22. R. J. Zhou, L. Q. Hu, Y. Zhang, G. Q. Zhong, S. Y. Lin, and The EAST Team, Nucl. Fusion **57**, 114002 (2017). https://doi.org/10.1088/1741-4326/aa7c9d
23. L. Zeng, Z. Y. Chen, Y. B. Dong, H. R. Koslowski, Y. Liang, Y. P. Zhang, H. D. Zhuang, D. W. Huang, and X. Gao, Nucl. Fusion **57**, 046001 (2017). https://doi.org/10.1088/1741-4326/aa57d9
24. M. Rubel, S. Brezinsek, J. W. Coenen, A. Huber, A. Kirschner, A. Kreter, P. Petersson, V. Philipps, A. Pospieszczyk, B. Schweer, G. Sergienko, T. Tanabe, Y. Ueda, and P. Wienhold, Matter Radiat. Extremes **2**, 87 (2017). https://doi.org/10.1016/j.mre.2017.03.002
25. A. J. Dai, Z. Y. Chen, D. W. Huang, R. H. Tong, J. Zhang, Y. N. Wei, T. K. Ma, X. L. Wang, H. Y. Yang, and H. L. Gao, Plasma Phys. Control. Fusion **60**, 055003 (2018). https://doi.org/10.1088/1361-6587/aab16d
26. J. Li and Y. Wan, J. Fusion Energy **38**, 113 (2019). https://doi.org/10.1007/s10894-018-0165-2
27. M. Vlainic, O. Ficker, J. Mlynar, E. Macusova, and The COMPASS Tokamak Team, Atoms **7** (1) (2019). https://doi.org/10.3390/atoms7010012
28. J. Zebrowski, L. Jakubowski, M. Rabinski, M. J. Sadowski, M. J. Jakubowski, R. Kwiatkowski, K. Malinowski, R. Mirowski, J. Mlynar, and O. Ficker, J. Phys.: Conf. Ser. **959**, 012002 (2018). https://doi.org/10.1088/1742-6596/959/1/012002
29. M. J. Sadowski, Nukleonika **56**, 85 (2011).
30. P. V. Savrukhin and E. A. Shestakov, Nucl. Fusion **55**, 043016 (2015). https://doi.org/10.1088/0029-5515/55/4/043016
31. A. M. Zaitsev, *Optical Properties of Diamond: A Data Handbook* (Springer Science, New York, 2013). https://doi.org/10.1007/978-3-662-04548-0
32. N. Yamamoto and H. Sugiyama, Radiat. Eff. Defects Solids **117**, 5 (1991). https://doi.org/10.1080/10420159108220585
33. N. Yamamoto, H. Sugiyama, and A. Toda, Proc. R. Soc. London, Ser. A **452**, 2279 (1996). https://doi.org/10.1098/rspa.1996.0122
34. D. A. Sorokin, A. G. Burachenko, D. V. Beloplotov, V. F. Tarasenko, E. Kh. Baksht, E. I. Lipatov, and M. I. Lomaev, J. Appl. Phys. **122**, 154902 (2017). https://doi.org/10.1063/1.4996965

35. A. G. Buranchenko, V. F. Tarasenko, D. V. Beloplotov, and E. Kh. Baksht, Russ. Phys. J. **60**, 1533 (2018). https://doi.org/10.1007/s11182-018-1247-3
36. E. I. Lipatov, K. R. Burumbayeva, D. E. Genin, V. S. Ripenko, M. A. Shulepov, and V. F. Tarasenko, in *Proceedings of the International Conference on Atomic and Molecular Pulsed Lasers XIII,* Proc. SPIE **10614**, 106141H (2018). https://doi.org/10.1117/12.2307089
37. V. I. Solomonov and S. G. Mikhailov, *Pulsed Cathodoluminescence and its Application for the Analysis of Condensed Matter* (UrO RAN, Yekaterinburg, 2003) [in Russian].
38. E. I. Lipatov, V. M. Lisitsyn, V. I. Oleshko, E. F. Polisadova, V. F. Tarasenko, and E. H. Baksht, in *Cathodoluminescence,* Ed. by N. Yamamoto (IntechOpen, Rijeka, Croatia, 2012), p. 51.
39. J. Dobrev and P. Markovic, *Calcite: Formation, Properties and Applications* (Nova Science, New York, 2012).
40. V. F. Tarasenko, V. I. Oleshko, M. V. Erofeev, E. I. Lipatov, D. V. Beloplotov, M. I. Lomaev, A. G. Burachenko, and E. Kh. Baksht, J. Appl. Phys. **125**, 244501 (2019). https://doi.org/10.1063/1.5094956
41. E. K. Baksht, A. V. Vukolov, M. V. Erofeev, G. A. Naumenko, A. P. Potylitsyn, V. F. Tarasenko, A. G. Burachenko, and M. V. Shevelev, JETP Lett. **109**, 564 (2019). https://doi.org/10.1134/S0021364019090078
42. V. F. Tarasenko, E. Kh. Baksht, D. V. Beloplotov, A. G. Burachenko, and M. I. Lomaev, Jpn. J. Appl. Phys. **59**, SHHD01 (2020). https://doi.org/10.35848/1347-4065/ab7475
43. A. M. Frelin, J. M. Fontbonne, G. Ban, J. Colin, M. Labalme, A. Batalla, A. Isambert, A. Vela, and T. Leroux, Med. Phys. **32**, 3000 (2005). https://doi.org/10.1118/1.2008487
44. K. W. Jang, T. Yagi, C. H. Pyeon, W. J. Yoo, S. H. Shin, C. Jeong, B. J. Min, D. Shin, T. Misawa, and B. Lee, J. Biomed. Opt. **18**, 027001 (2013). https://doi.org/10.1117/1.JBO.18.2.027001
45. B. Lee, S. H. Shin, W. J. Yoo, and K. W. Jang, Opt. Rev. **23**, 806 (2016). https://doi.org/10.1007/s10043-016-0240-8
46. Y. N. Kharzheev, Phys. Part. Nucl. **50**, 42 (2019). https://doi.org/10.1134/S1063779619010027
47. F. Therriault-Proulx, L. Beaulieu, L. Archambault, and S. Beddar, Phys. Med. Biol. **58**, 2073 (2013). https://doi.org/10.1088/0031-9155/58/7/2073
48. L. P. Babich, T. V. Loiko, and A. V. Rodigin, Dokl. Phys. **59**, 351 (2014). https://doi.org/10.1134/S1028335814080102
49. L. P. Babich, T. V. Loiko, and A. V. Rodigin, IEEE Trans. Plasma Sci. **42**, 948 (2014). https://doi.org/10.1109/TPS.2014.2308529
50. E. K. Baksht, A. G. Burachenko, D. V. Beloplotov, and V. F. Tarasenko, Russ. Phys. J. **59**, 484 (2016). https://doi.org/10.1007/s11182-016-0798-4
51. V. F. Tarasenko, E. Kh. Baksht, A. G. Burachenko, D. V. Beloplotov, and A. V. Kozyrev, IEEE Trans. Plasma Sci. **45**, 76 (2017). https://doi.org/10.1109/TPS.2016.2637570
52. V. I. Oleshko, E. K. Baksht, A. G. Burachenko, and V. F. Tarasenko, Tech. Phys. **62**, 299 (2017). https://doi.org/10.1134/S1063784217020232
53. A. P. Cherenkov, Dokl. Akad. Nauk SSSR **2**, 451 (1934). https://doi.org/10.3367/UFNr.0093.196710n.0385
54. S. I. Vavilov, Dokl. Akad. Nauk SSSR **2**, 457 (1934). https://doi.org/10.3367/UFNr.0093.196710m.0383
55. I. E. Tamm and I. M. Frank, Dokl. Akad. Nauk SSSR **14**, 107 (1937). https://doi.org/10.3367/UFNr.0093.196710o.0388
56. J. V. Jelly, *Cherenkov Radiation and its Applications* (Pergamon, London, 1958).
57. V. P. Zrelov, *Vavilov-Cherenkov Radiation and its Application in High-Energy Physics, Part 1* (Atomizdat, Moscow, 1968) [in Russian].
58. V. I. Bespalov, *Interaction of Ionizing Radiation with Matter* (Tomsk. Politekh. Univ., Tomsk, 2008) [in Russian].
59. E. A. Stroganova, I. N. Parshina, M. A. Kiekpaev, and P. A. Ponomareva, *Organic Chemistry. Part 2. Methods of Isolation, Purification and Identification of Organic Compounds, Practical Guide* (OGU, Orenburg, 2013) [in Russian].
60. D. A. Sorokin, A. G. Burachenko, V. F. Tarasenko, E. Kh. Baksht, and M. I. Lomaev, Instrum. Exp. Tech. **61**, 262 (2018). https://doi.org/10.1134/S0020441218020240
61. I. D. Kostyrya, D. V. Rybka, and V. F. Tarasenko, Instrum. Exp. Tech. **55**, 72 (2012). https://doi.org/10.1134/S0020441212010071
62. V. F. Tarasenko, I. D. Kostyrya, E. Kh. Baksht, and D. V. Rybka, IEEE Trans. Dielectr. Electr. Insul. **18**, 1250 (2011). https://doi.org/10.1109/TDEI.2011.5976123
63. V. F. Tarasenko, S. B. Alekseev, E. K. Baksht, A. G. Burachenko, and M. I. Lomaev, Instrum. Exp. Tech. **63**, 359 (2020). https://doi.org/10.1134/S0020441220040090
64. G. A. Mesyats, S. D. Korovin, V. V. Rostov, and V. G. Shpak, Proc. IEEE **92**, 1166 (2004). https://doi.org/10.1109/JPROC.2004.829005
65. V. F. Tarasenko, Plasma Phys. Rep. **37**, 409 (2011). https://doi.org/10.1134/S1063780X11040118
66. E. H. Baksht, A. G. Burachenko, V. Yu. Kozhevnikov, A. V. Kozyrev, I. D. Kostyrya, and V. F. Tarasenko, J. Phys. D **43**, 305201 (2010). https://doi.org/10.1088/0022-3727/43/30/305201
67. A. G. Burachenko and V. F. Tarasenko, Tech. Phys. Lett. **36**, 1158 (2010). https://doi.org/10.1134/S1063785010120278
68. M. I. Yalandin and V. G. Shpak, Instrum. Exp. Tech. **44**, 285 (2001). https://doi.org/10.1023/A:1017535304915
69. V. F. Tarasenko and D. V. Rybka, High Voltage **1**, 43 (2016). . https://doi.org/10.1049/hve.2016.0007
70. V. F. Tarasenko, E. Kh. Baksht, A. G. Burachenko, M. I. Lomaev, and D. A. Sorokin, IEEE Trans. Plasma Sci. **38**, 2583 (2010). https://doi.org/10.1109/TPS.2010.2041474

71. G. A. Naumenko, A. P. Potylitsyn, P. V. Karataev, M. A. Shipulya, and V. V. Bleko, JETP Lett. **106**, 127 (2017). https://doi.org/10.1134/S0021364017140089
72. V. I. Oleshko, V. F. Tarasenko, D. V. Beloplotov, and S. S. Vil'chinskaya, Opt. Spectrosc. **125**, 627 (2018). https://doi.org/10.1134/S0030400X18110218
73. V. F. Tarasenko, E. K. Baksht, D. V. Beloplotov, A. G. Burachenko, M. V. Erofeev, E. I. Lipatov, M. I. Lomaev, and V. I. Oleshko, Russ. Phys. J. **62**, 1181 (2019). https://doi.org/10.1007/s11182-019-01833-6
74. A. G. Burachenko, D. V. Beloplotov, I. A. Prudaev, D. A. Sorokin, V. F. Tarasenko, and O. P. Tolbanov, Opt. Spectrosc. **123**, 867 (2017). https://doi.org/10.1134/S0030400X17110042
75. A. Kuramata, K. Koshi, S. Watanabe, Y. Yamaoka, T. Masui, and S. Yamakoshi, Jpn. J. Appl. Phys. **55**, 1202A2 (2016). https://doi.org/10.7567/JJAP.55.1202A2
76. E. K. Baksht, M. V. Erofeev, V. F. Tarasenko, M. I. Solomonov, and V. A. Shitov, Russ. Phys. J. **63**, 1150 (2020). https://doi.org/10.1007/s11182-020-02165-6
77. V. V. Osipov, Y. A. Kotov, M. G. Ivanov, O. M. Samatov, V. V. Lisenkov, V. V. Platonov, A. M. Murzakaev, A. I. Medvedev, and E. I. Azarkevich, Laser Phys. **16**, 116 (2006). https://doi.org/10.1134/S1054660X06010105
78. Refractive Index Database. https://refractiveindex.info.
79. Electro Glass. http://www.elektrosteklo.
80. Optical Technological Laboratory. https://opto-tl.ru/materials/crystals_glass_reference_information.
81. M. I. Lomaev, E. A. Sosnin, and V. F. Tarasenko, Prog. Quantum Electron. **36**, 51 (2012). https://doi.org/10.1016/j.pquantelec.2012.03.003
82. E. I. Lipatov, D. E. Genin, D. V. Grigor'ev, V. F. Tarasenko, A. G. Burachenko, E. Kh. Baksht, and D. V. Beloplotov, AIP Conf. Proc. **2069**, 040007 (2019). https://doi.org/10.1063/1.5089850
83. V. F. Tarasenko, M. I. Lomaev, E. Kh. Baksht, D. V. Beloplotov, A. G. Burachenko, D. A. Sorokin, and E. I. Lipatov, Matter Radiat. Extremes **4**, 037401 (2019). https://doi.org/10.1063/1.5096563
84. E. K. Baksht, A. G. Burachenko, and V. F. Tarasenko, Tech. Phys. Lett. **36**, 1020 (2010). https://doi.org/10.1134/S1063785010110143
85. V. V. Plyusnin, L. Jakubowski, J. Zebrowski, P. Duarte, K. Malinowski, H. Fernandes, C. Silva, M. Rabinski, and M. J. Sadowski, Rev. Sci. Instrum. **81**, 10D304 (2010). https://doi.org/10.1063/1.3478658
86. E. I. Lipatov, V. M. Lisitsyn, V. I. Oleshko, and V. F. Tarasenko, Russ. Phys. J. **50**, 52 (2007). https://doi.org/10.1007/s11182-007-0005-8
87. D. Takeuchi, H. Watanabe, S. Yamanaka, H. Okushi, H. Sawada, H. Ichinose, T. Sekiguchi, and K. Kajimura, Phys. Rev. B **63**, 245328 (2001). https://doi.org/10.1103/PhysRevB.63.245328
88. E. A. Vasil'ev, V. I. Ivanov-Omskii, B. S. Pomazanskii, and I. N. Bogush, Tech. Phys. Lett. **30**, 802 (2004). https://doi.org/10.1134/1.1813714
89. A. S. Nasibov, in *Generation of Runaway Electrons and X-Rays in High-Pressure Discharges* (STT, Tomsk, 2015), p. 297 [in Russian].
90. K. Takiyama, M. I. Abd-Elrahman, T. Fujita, and T. Oda, Solid State Commun. **99**, 793 (1996). https://doi.org/10.1016/0038-1098(96)00309-2
91. E. I. Lipatov, D. E. Genin, D. V. Grigor'ev, and V. F. Tarasenko, in *Luminescence - An Outlook on the Phenomena and their Applications,* Ed. by J. Thirumalai (IntechOpen, Rijeka, Croatia, 2016), p. 191.
92. M. V. Erofeev, E. K. Baksht, V. I. Oleshko, and V. F. Tarasenko, Russ. Phys. J. **63**, 831 (2020). https://doi.org/10.1007/s11182-020-02105-4
93. L. Lisitsyna, V. I. Korepanov, and T. V. Grechkina, Opt. Spectrosc. **95**, 746 (2003). https://doi.org/10.1134/1.1628723
94. V. F. Tarasenko, E. K. Baksht, A. G. Burachenko, D. V. Beloplotov, and A. V. Kozyrev, Dokl. Phys. **61**, 539 (2016). https://doi.org/10.1134/S1028335816110082
95. E. K. Baksht, K. P. Artemov, A. G. Burachenko, and V. F. Tarasenko, Opt. Spectrosc. **127**, 694 (2019). https://doi.org/10.1134/S0030400X19100047
96. Z. A. Al'bikov, A. I. Veretennikov, and O. V. Kozlov, *Pulsed Ionizing Radiation Detectors* (Atomizdat, Moscow, 1978) [in Russian].
97. B. Lee, G. Kwon, S. H. Shin, J. Kim, W. J. Yoo, Y. H. Ji, and K. W. Jang, Sensors **15**, 29003 (2015). https://doi.org/10.3390/s151129003
98. K. W. Jang, W. J. Yoo, J. K. Seo, J. Y. Heo, J. Moon, J.-Y. Park, E. J. Hwang, D. Shin, S.-Y. Park, H.-S. Cho, and B. Lee, Nucl. Instrum. Methods Phys. Res., Sect. A **652**, 841 (2011). . https://doi.org/10.1016/j.nima.2010.08.120
99. V. F. Tarasenko, E. K. Baksht, and M. V. Erofeev, Tech. Phys. Lett. **47** (3), 267 (2021).
100. T. Afsari, M. Ghoranneviss, S. Meshkani, and M. R. Ghanbari, J. Theor. Appl. Phys. **14**, 101 (2020). https://doi.org/10.1007/s40094-019-00366-0
101. J. R. Dwyer, Z. Saleh, H. K. Rassoul, D. Concha, M. Rahman, V. Cooray, J. Jerauld, M. A. Uman, and V. A. Rakov, J. Geophys. Res.: Atmos. **113**, D23207 (2008). https://doi.org/10.1029/2008JD010315
102. E. I. Lipatov, V. F. Tarasenko, M. V. Erofeev, V. S. Ripenko, and M. A. Shulepov, Atmos. Ocean. Opt. **33**, 195 (2020). https://doi.org/10.1134/S1024856020020049

Translated by A. Nikol'skii